

# We are IntechOpen, the world's leading publisher of Open Access books Built by scientists, for scientists

6,900

Open access books available

185,000

International authors and editors

200M

Downloads

Our authors are among the

154

Countries delivered to

TOP 1%

most cited scientists

12.2%

Contributors from top 500 universities



WEB OF SCIENCE™

Selection of our books indexed in the Book Citation Index  
in Web of Science™ Core Collection (BKCI)

Interested in publishing with us?  
Contact [book.department@intechopen.com](mailto:book.department@intechopen.com)

Numbers displayed above are based on latest data collected.  
For more information visit [www.intechopen.com](http://www.intechopen.com)



---

# Effects of Solar Radio Emission and Ionospheric Irregularities on GPS/GLONASS Performance

---

Vladislav V. Demyanov, Yury V. Yasyukevich and Shuanggen Jin

Additional information is available at the end of the chapter

<http://dx.doi.org/10.5772/54568>

---

## 1. Introduction

During the period of 2001-2010, several strong geomagnetic storms and direct solar radio emission interference deteriorated serious GPS performance. The L-band solar radio emission has recently been regarded as a potential threat to stable GPS and GLONASS performance. However, the threat has not been completely investigated or assessed so far. Furthermore, ionization anomaly at low latitudes along with the effect of the equatorial plasma “bubbles” increase the possibility of fading for transionospheric signals, especially during geomagnetic storms. Instabilities of ionospheric plasma on the “walls” of a bubble with electron density lower than the background value are also characterized by sharp gradients of electron density. For example, the walls of bubbles can be a source of ionospheric scintillations as well. Therefore, the spatial orientation of plasma bubble plays a decisive role in strengthening and weakening the amplitude and phase scintillations of satellite vehicle (SV) signals.

Although GPS ranging and positioning failures were investigated under such unfavorable geophysical conditions, but their exact nature remains unclear. This chapter is devoted to some features of GPS/GLONASS performance under specific geophysical events such as solar radio emission bursts and strong satellite signal scattering from the equatorial plasma “bubbles”. As irregularities are elongated in the magnetic field direction, a ray path that is parallel to the magnetic field incorporates a greater path length through depleted regions containing plasma density irregularities. We propose a GPS method to detect mid-latitude field-aligned irregularities (FAIs) by line-of-sight angular scanning regarding the local magnetic field vector. Using GPS data of the Japanese GPS network (GEONET), we analyze occurrence of GPS-phase slips and positioning errors during the geomagnetic storm of February 12, 2000.

In addition, it is very important to provide the stable performance of GPS (GLONASS) receiver under strong geomagnetic storms. The scintillation index  $S_4$  is suggested as an adequate indicator of the current media state along the each satellite vehicle (SV) line-of-sight when the significant small scale ionospheric irregularities are present. To prove this idea we further conduct positioning measurements on a basis of combined GPS/GLONASS receiver (MRC-19L) as well as the measurements of the current ionosphere state during the strong magnetic storm on November 9, 2004.

## 2. Solar radio emission power threat on GPS and GLONASS

Until recently the L-band solar radio emission was not considered as a potential threat to the stable performance of satellite radio navigation systems such as GPS and GLONASS (Chen et al., 2005; Jin et al., 2008). Power threshold of the solar radio emission at the level of 40.000 sfu (solar flux units), which still provided steady performance of GPS, was found by Klobuchar et al. (1999). However only several solar radio bursts with the power level higher than 40.000 sfu have been observed over the last 40 years (Cerruti et al., 2006; Chen et al., 2005). According to Carrano et al. (2007), the signal-to-noise ratio decreases by 10-30 dB depending on the angular position of the sun relative to the directional pattern of receiver antenna under the direct influence of the solar radio emission. It causes failure in signal tracking of many visible navigation satellites on the earth's dayside for up to 1 hour.

Detailed investigation of the direct of solar radio emission interference on the GPS equipment performance indicated that the unsafe threshold of the solar radio emission power should be reduced to 4.000-12.000 sfu. A specific value of this threshold should be determined according to the type of signal tracking algorithms which are utilized in GPS/GLONASS user equipment. As it was proven by Afraimovich et al. (2008) and Cerruti et al. (2006), many short-term failures in measurements of radio navigation parameters were observed in GPS and GPS/GLONASS receivers all over the world during strong solar radio bursts on December 6 and 13, 2006. Some failures in measurements of radio navigation parameters were recorded even when the solar radio flux power was as much as  $3 \cdot 10^3$  sfu (Afraimovich et al., 2008).

Nevertheless, a detailed analysis of separate solar radio bursts impact on the GPS/GLONASS user navigation equipment is required in order to estimate an extent of deterioration of the positioning systems on a global scale. Especially, maximum allowable power of the solar radio emission, which provides satisfactory signal-to-noise ratio at the navigation receiver input, is also very important. Such research would allow us to reestimate GPS and GLONASS noise immunity and make necessary improvements into navigation receivers development according to the known impact of the solar radio emission. The aim of section 2 is to evaluate the unsafe threshold of solar radio emission power for GPS/GLONASS receivers on a basis of theoretical and experimental analysis of the potential noise immunity of GLONASS standard precision code (SP) and high precision code (HP) with comparison to GPS CA (P(Y)) dual - frequency receivers.

## 2.1. The solar radio emission power at GPS/GLONASS receiver antenna output

The steady operation of a GPS/GLONASS receiver under the influence of intensive radio interference depends on the characteristics of radiofrequency (RF) path of navigation receiver within which the main filtering and amplification of satellite signals take place. The exact measurement of solar radio emission power, which affects the radiofrequency path input, is therefore very important. This measurement is necessary to design optimal algorithms for primary processing and filtering of radio-navigation parameters in the processor of navigation receiver.

Computing of solar radio emission power at the radiofrequency path input should begin with consideration of the receiver antenna directional pattern. The antenna directive gain (AD) is defined as ratio between the power specified for a real antenna  $P(\theta, \alpha)$  and the power specified for a reference isotropic antenna ( $P_0$ ), provided that signal powers at the observation point are equal.

$$D(\theta, \alpha) = P(\theta, \alpha) / P_0 \quad (1)$$

where  $\theta$  and  $\alpha$  are azimuth and elevation of line-of-sight (LOS).

First we should set the characteristics of directional properties of a real receiving antenna. The characteristics are the receiving antenna power gain  $G(\theta)$  relative to the ideal isotropic antenna (Table 1, column 2) and the antenna directive gain  $D(\theta, \alpha)$  (Table 1, column 3)

$$G(\theta) = 10 \cdot \lg(D(\theta, \alpha)) \quad (2)$$

Elevation of signal reception $\theta$ (deg.)	$G(\theta)$ (dB)	$D(\theta, \alpha) = P(\theta, \alpha) / P_0$
$0 < \theta < 5$	$-7.5 \leq G(\theta) \leq -5$	$0.1775 \leq D(\theta, \alpha) \leq 0.316$
$5 < \theta < 15$	$-4.5 \leq G(\theta)$	$0.354 \leq D(\theta, \alpha)$
$\theta > 15$	$-2 \leq G(\theta)$	$0.63 \leq D(\theta, \alpha)$

**Table 1.** Directive characteristics of a navigation receiver antenna (Kaplan, 1996)

Another property of the receiving antenna to be considered for performing calculations is the antenna effective area. AD values is related to the antenna effective area by

$$D(\theta, \alpha) = 4\pi \cdot A_e(\theta) / \lambda^2 \quad (3)$$

where  $\lambda$  is the signal wavelength and  $A_e$  is the antenna effective area. Equation (3) implies that the real receiving antenna has AD in the azimuthal plane equal to that of the standard isotropic antenna, i.e. the value of  $D(\theta, \alpha)$  does not depend on the azimuth  $\alpha$  of the received signal. Its

elevation dependence has already taken into account in Table 1. Thus, we can calculate the magnitudes of effective area of the real receiver antenna at two operating frequencies of GPS/GLONASS and different elevations. Table 2 contains calculation results for GPS operating frequencies. In our further consideration we assume that the  $A_e$  values for GLONASS receivers are close to GPS ones.

$\theta, ^\circ$	$A_e(\theta), \text{m}^2$	
	$\lambda_{L1} = 0.1903 \text{ m}$	$\lambda_{L2} = 0.2442 \text{ m}$
$0^\circ < \theta < 5^\circ$	$5.099 \cdot 10^{-4} \leq A_e(\theta) \leq 9.077 \cdot 10^{-4}$	$8.409 \cdot 10^{-4} \leq A_e(\theta) \leq 1.497 \cdot 10^{-3}$
$5^\circ < \theta < 15^\circ$	$1.01 \cdot 10^{-3} \leq A_e(\theta)$	$1.677 \cdot 10^{-3} \leq A_e(\theta)$
$\theta > 15^\circ$	$1.809 \cdot 10^{-3} \leq A_e(\theta)$	$2.984 \cdot 10^{-3} \leq A_e(\theta)$

**Table 2.** Antenna effective area

After determining the main characteristics of the receiving antenna, we can compute the power of the solar radio emission at the receiving antenna output. In order to do this the following specifications and assumption were taken into account:

Solar radio emission flux with the power of 1 sfu is equal to the power spectral density corresponding to the interval of 1 Hz of this flux power spectrum passing through the area of 1 m<sup>2</sup>, i.e. 1 sfu = 10<sup>-22</sup> W m<sup>-2</sup> Hz<sup>-1</sup> (Chen et al., 2005).

Radio emission of the solar flare relative to an actual satellite signal is considered as the white Gaussian noise. Generally the noise power  $P_n$  within the given frequency band from  $F_1$  to  $F_2$  is obtained from the noise spectrum  $S(f)$  as follows

$$P_n = \int_{F_1}^{F_2} S(f) df \quad (4)$$

The solar radio emission intensity  $N_0$  in the frequency band  $\Delta F_n$  of the satellite signal is constant throughout the band. So the radio emission power of a solar flare within the frequency bands of GPS and GLONASS signals can be computed in the similar way as follows

$$P_n = \Delta F_n \cdot N_0 \quad (5)$$

The solar radio noise has the right hand elliptical polarization and undergoes attenuation proportional to the polarization mismatch factor of 3.4 dB (at the frequency L1) and 4.4 dB (at the frequency L2) when passing through the antenna (ICD-GPS-200c, 1993);

When passing through the atmosphere, the solar radio emission in the GPS (GLONASS) frequency band undergoes the maximum attenuation of -2 dB (ICD-GLONASS, 2002; ICD-GPS-200c, 1993);

Thus, without considering polarization loss and attenuation in the atmosphere the power of the solar radio noise  $P_n$  at the receiving antenna output can be defined as:

$$P_{n,GPS(GLN)} = \Delta F_{n,GPS(GLN)} \cdot k \cdot N_0 \cdot A_e(\theta) \quad (6)$$

where  $k$  is the rate of the solar radio emission flux and  $N_0 = 10^{-22} \text{ W m}^{-2} \text{ Hz}^{-1}$ .

The value of the solar radio emission power also depends on the sun zenith angle. In Eq. (6), this dependence is expressed in implicit form in terms of  $A_e(\theta)$  (Table 2). Since it is more convenient to use power units (dBW) for further analysis, the solar radio noise power at the receiving antenna output may be converted to these units as

$$L_{n,GPS(GLN)} = 10 \cdot \lg(P_{n,GPS(GLN)}) \quad (7)$$

If we take into account the polarization loss and attenuation in the atmosphere at the frequencies L1 and L2 (ICD-GPS-200c, 1993) we get  $L_{n1,GPS(GLN)} = 10 \cdot \lg(P_{n1,GPS(GLN)}) - 2 - 3.4$  and  $L_{n2,GPS(GLN)} = 10 \cdot \lg(P_{n2,GPS(GLN)}) - 2 - 4.4$ , at the frequencies L1 and L2, respectively.

Finally, we can compute the solar radio noise power at the receiving antenna output for sun elevation  $>15^\circ$  at the central solar radio emission frequency  $f=1415 \text{ MHz}$  (we assumed  $\lambda=0.212 \text{ m}$ ,  $A_e = 2.25310^{-3} \text{ m}^2$ , polarization loss = -3.4dB) in Table 3.

The front-end passband of the GPS receiver radio path ( $\Delta F_{GPS}$ ) is 3 MHz (Kaplan, 1996), while the passband of the GLONASS receiver for the channel of each separate satellite is only 0.5 MHz ( $\Delta F_{GLN}$ ) (Perov and Kharisov, 2005). Hence power of solar radio emission should be considered only in these narrow frequency bands for GPS and GLONASS correspondingly (Table 3).

The solar radio emission						
flux $k$ , sfu	1	$10^2$	$10^3$	$10^4$	$10^5$	$10^6$
$L_n$ , dBW						
$L_{n,GPS}$ , dBW ( $\Delta F_{GPS}=3 \text{ MHz}$ )	-187.1	-167.1	-157.1	-147.1	-137.1	-127.1
$L_{n,GLN}$ , dBW ( $\Delta F_{GLN}=0.5 \text{ MHz}$ )	-194.8	-174.8	-164.8	-154.8	-144.8	-134.8

**Table 3.** Rate of the solar radio emission flux

Here we should provide some special explanation about the front-end passband of the GPS and GLONASS radiofrequency chain. Generally the front-end band width should be twice the chipping rate - 1.023 MHz for GPS and 0.511 MHz for GLONASS (Perov and Kharisov, 2005; Tsui, 2005). However, depending on the navigation receiver specification the bandwidth can be set significantly larger or lower. Moreover, we should take into account that a navigation receiver utilizes the same RF path in order to process CA and P(Y) code signals concurrently at the same current frequency (1.5 GHz for GPS and 1.6 GHz for GLONASS). Hence we can not set RF front-end band width too narrow because it can cause severe phase distortion of the P(Y) or HP signal. On the other hand, we should keep the bandwidth narrow enough for effective suppressing of external radio noise including the solar radio emission. The specific choice depends on the developer of the GPS/GLONASS receiver specification, while it is unknown for us exactly. In order to evaluate the effect of solar radio emission on navigation receivers we used some averaged values of the RF front-end bandwidth (Table 3).

Generally, it is known that GLONASS utilizes frequency division multiple access (FDMA) technology to separate the signals of particular GLONASS satellites. It requires to set narrower RF front-end bandwidth in comparing to GPS one. The main expected consequence is lower integral solar radio noise power at the AD converter input of the navigation receiver. A comparative plot between powers of GPS and GLONASS received signals and the solar radio emission  $P_{SFU}$  at the output of receiving antenna can be made on the basis of above mentioned reasons. Fig. 1a gives the ratio of powers of the solar radio emission flux and GPS signal components and Fig. 1b illustrates the same for GLONASS.

The horizontal lines in Fig. 1a indicate levels of minimum (red lines) and maximum (black lines) power of GPS signal components at the receiving antenna output (ICD-GPS-200c, 1993). The power levels for the components of coarse acquisition code – CA (P(CA)) and encrypted P(Y)- code (P(P(Y))) at the L1 frequency, and for the P(Y) component at the L2 frequency are presented by dashed lines, dots and solid lines, respectively. The slant line shows power values of the solar radio emission flux  $P_{SFU}$ . Fig. 1b has the same notations for the components of the standard precision code and high precision code of GLONASS signals at frequencies L1 and L2 (ICD-GLONASS, 2002). As power values of some components are close, these lines partially mix in the diagram. The power values of the solar radio emission flux in terms of sfu are plotted along the horizontal axis with the logarithmic scale.

It is obvious from Fig. 1 for a solar radio noise within  $10^2 - 10^4$ , the power of the solar radio noise is compared with power of the satellite signal at the receiving antenna output and exceeds it. When the solar radio emission flux is  $10^6$  sfu, the level of the solar radio noise exceeds the signal by 26-39 dB at the GPS receiving antenna output and by 20-32 dB at the GLONASS receiving antenna output.

## 2.2. Unsafe threshold of the solar radio emission power for GPS and GLONASS

Based on the above mentioned estimates, we can determine the unsafe threshold of solar radio noises at which the signal-to-noise ratio at the receiving antenna output is insufficient for stable tracking of satellite signals. First, we should take into account the fact that a significant gain in the signal-to-noise ratio is observed due to the use of correlation processing of the received

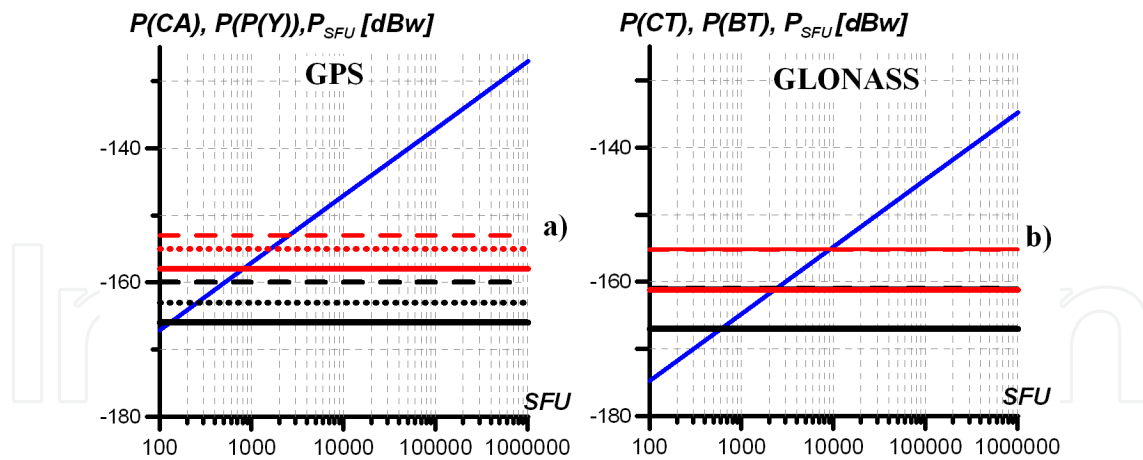


**Figure 1.** Power level of the solar radio emission at the receiving antenna output

signals if the structure of the pseudonoise ranging code is known at the receiving site. This gain (in terms of dBW) can be calculated as follows (Kaplan, 1996)

$$SN_{cor} = 10 \cdot \lg\left(\frac{F_{PRN}}{2 \cdot \Delta F_{PD}}\right) \quad (8)$$

where  $F_{PRN}$  is the frequency of elementary pulse in pseudorandom sequences of ranging code:  $F_{PRN} = 1.023$  MHz for the CA code and 10.23 MHz for the P(Y) code of GPS, or 0.511 MHz for the SP code and 5.11 MHz for the HP code of GLONASS, respectively;  $\Delta F_{PD}$  is the predetector passband that is found from the lowest modulation frequency of the satellite signal by the service information data (50 Hz) (Kaplan, 1996; Perov and Kharisov, 2005).

Since the CA (SP) code structure is always known, it is obvious that GPS and GLONASS maximum noise immunity under the influence of a powerful solar radio emission takes place for the CA (SP) code at the main operating frequency L1. On the other hand, L2 GPS signal is only modulated by the encrypted code. “Semicodeless” or “codeless” processing algorithms are widely used in dual-frequency receivers in order to extract the P(Y) or HP-code signal components at the L2 GPS (GLONASS) frequency. Usage of these algorithms with no sufficient data on the P(Y) or HP -code structure reduces the stability of signal tracking at the L2 frequency under the influence of external radio emission (Skone and Jong, 2001). Significant fading of the signal-to-noise ratio while the encrypted signal is extracting and tracking at the L2 frequency may take place depending on the type of correlation processing algorithm. The level of these losses in the signal-to-noise ratio  $\Delta SN_{cor}$  is within 14 - 17 dB (if “semicodeless” algorithms are utilized) and 27 - 30 dB (with the use of “codeless” algorithms) (Chen et al., 2005).

Access to the HP signal component of GLONASS and to the P(Y) code in the GPS system is not for common use, and in our examination we suppose that the correlation losses of HP signal tracking at L2 GLONASS frequency are equal to ones of GPS. It is known, that integration time periods in phase and code tracking loops of GPS (GLONASS) receivers inside the

“integrate and dump” module are approximately the same: 1 ms – in the phase tracking loop and 20 ms – in the code tracking loop. The origin of the distortion of the correlation integral under “semicodeless” or “codeless” processing technique for both GPS and GLONASS is the same. Hence we suppose that correlation losses  $\Delta SN_{cor}$  should also be approximately the same.

When the satellite signal is locked the coherent tracking of the carrier frequency phase and code delay of the signal starts. The noise immunity of a navigation receiver is defined by the noise immunity level of the phase lock loop (PLL) of the receiver (Kaplan, 1996). That is why the unsafe threshold of solar radio emission, causing the satellite signal tracking loss, should be determined from the level of minimum acceptable signal-to-noise ratio that provides stable performance of the PLL.

The discrimination characteristics of the phase discriminator has a limited linear section, therefore severe requirements are imposed on the maximal acceptable carrier phase filtering error  $\sigma_{\phi, max}$ . If the error level is exceeded, phase filtration is divergent and the signal tracking loss is observed. Magnitude of filtering error  $\sigma_{\phi}$  of the carrier phase depends on many factors such as receiver thermal noises, short-term instability of reference generator frequency and phase fluctuation, caused by dynamic impact on the navigation satellite. With all the above consideration, we can determine filtering error magnitude of the carrier phase as follows (Kaplan, 1996),

$$\sigma_{\phi} = \sqrt{\sigma_T^2 + \sigma_F^2} + \frac{\sigma_s}{3} \leq \sigma_{\phi, max} \quad (9)$$

where  $\sigma_T$ ,  $\sigma_F$ , and  $\sigma_s$  are root-mean-square (RMS) of the carrier phase filtration (in degrees) error caused by thermal noises, short-term instability of the reference generator frequency, and dynamic stress of the receiver, respectively. The magnitudes of separate components of (9) can be calculated from the following formulae (Kaplan, 1996),

$$\sigma_T = \frac{360}{2 \cdot \pi} \sqrt{\frac{\Delta F_{PLL}}{cn_0} \cdot \left[ 1 + \frac{1}{2T_{COR} \cdot cn_0} \right]} \quad (10)$$

where  $\Delta F_{PLL}$  is the noise bandwidth of PLL,  $cn_0$  is the signal-to-noise ratio at the receiver input, expressed by the power ratio determined on the basis of the receiver sensitivity and,  $T_{COR}$  is the pre-detection integration time. The rms of error for the short-term instability of reference generator frequency is

$$\sigma_F = 160 \cdot \frac{\sigma_F(\tau) \cdot F_c}{\Delta F_{PLL}} \quad (11)$$

where  $F_c$  is the satellite signal carrier frequency. The rms of error for the dynamic stress of the receiver is

$$\sigma_s = 0.4828 \cdot \frac{dR^3/dt^3}{(\Delta F_{PLL})^3} \quad (12)$$

where  $dR^3/dt^3$  is the maximum dynamic stress of the receiver along the "satellite-receiver" line of sight. Expressions (11) and (12) are written for the third-order loop filter which is typically used for signal phase tracking in navigation receivers.

From (9) - (12) we can find an expression which defines the minimal allowable signal-to-noise ratio at the receiver input ( $CN_{thr}$  - in terms of dBW) for the maximum allowable value of the phase filtering error ( $\sigma_{\phi,max}$  - in terms of degrees) as follows,

$$CN_{thr} = -10 \cdot \lg \left[ T_{COR} \cdot \sqrt{1 + \frac{2B}{T_{COR} \Delta F_{PLL}}} - T_{COR} \right] \quad (13)$$

$$B = \left( \frac{2\pi}{360} \right)^2 \cdot \left[ (\sigma_{\phi,max} - \frac{\sigma_s}{3})^2 - \sigma_F^2 \right]$$

Next we can determine an equivalent signal-to-noise ratio at the receiver input under the influence of solar radio emission using the following equation (Kaplan, 1996),

$$CN_{eq} = -10 \cdot \lg \left[ 10^{-0.1CN_0} + \frac{10^{0.1JS}}{r \cdot Q \cdot F_{PRN}} \right] \quad (14)$$

where  $CN_0 = 10 \cdot \lg(P_{min})$  is the signal-to-noise ratio in terms of dBW at the receiver input, determined for the minimum power of the received signal,  $Q$  is the parameter of the spectral distribution of the external radio emission relative to the desired signal spectrum ( $Q=1$  for a narrow-band interference and  $Q=2$  for a wide-band Gaussian interference),  $JS$  is the relationship between the jamming solar radio emission power and the satellite signal power (dBW) and  $r$  is the coefficient considering distortion of the correlation integral when using "semi-codeless" or "codeless" technique for encrypted P(Y) or HP-code signal extracting.

The coefficient  $r$  can be calculated as follow

$$r = \frac{2\Delta F_{PD}}{F_{PRN}} 10^{0.1(SN_{cor} - \Delta SN_{cor})} \quad (15)$$

Here the gain in the signal-to-noise ratio due to the correlation processing  $SN_{cor}$  can be determined from (8), while the value of the correlation processing losses  $\Delta SN_{cor}$  is defined as difference between signal-to-noise ratio of ideal and real correlation receivers. The approximate  $\Delta SN_{cor}$  values were given above for "semi-codeless" and "codeless" correlation techniques (Chen et al., 2005).

It is interesting to know how solar radiation flux is related to the "ambient noise floor" of the GPS/GLONASS receiver. It would allow us to assess how many "extra sfus" are required to

get a certain signal-to-noise ratio decrease with noise figures of the given radio frequency chain. In order to achieve this goal we need to determine the value of the unjammed signal-to-noise ratio  $CN_0$  in terms of dBW taking into account all the total ambient noise figure sources as follows (Kaplan, 1996),

$$CN_0 = P_{\min} + G(\beta) - 10 \lg(m \cdot T_0) - N_f - L \quad (16)$$

where  $P_{\min}$  - is the minimal received signal power in dBW, determined according to the Interface Control Documents of GPS or GLONASS,  $G(\theta)$  is the receiving antenna power gain (Table 1), the term  $10 \cdot \lg(m \cdot T_0)$  is the ambient thermal noise density at the temperature of  $T_0$  (K),  $m=1.38 \cdot 10^{-23}$  (W·s/K) is the Boltzman's constant,  $N_f$  is the noise figure of receiver that includes antenna and cable losses in units of dB and  $L$  denotes the implementation losses, including AD converter loss in dB.

Finally, we can determine the unsafe threshold of solar radio emission power, which could cause GPS and GLONASS navigation satellite signals tracking loss under the given characteristics of the navigation receiver performance. Table 4 presents standard conditions of the GPS and GLONASS receiver performance (Kaplan, 1996; Perov and Kharisov, 2005) with estimated threshold signal-to-noise ratio.

Characteristics	Parameter value
Noise bandwidth of the third-order phase lock loop (Kaplan, 1996)	$\Delta F_{PLL} = 18$ Hz
Allan deviation oscillator phase noise (Kaplan, 1996)	$\sigma_p(\tau) = 10^{-10}$
Maximal line-of-sight jerk dynamics	$dR^3/dt^3 = 0$ m <sup>3</sup> /s <sup>3</sup>
Pre-detection integration time (Kaplan, 1996)	$T_{COR} = 20$ ms
Front-end passband of GPS receiver (Kaplan, 1996)	$\Delta F_{GPS} = 3$ MHz
Front-end passband of GLONASS receiver (for each satellite) (Perov and Kharisov, 2005)	$\Delta F_{GLN} = 0.5$ MHz
Correlation losses for "semicodeless" correlation techniques (Chen et al., 2005)	$\Delta SN_{cor} = 17$ dB
Correlation losses for "codeless" correlation techniques (Chen et al., 2005)	$\Delta SN_{cor} = 27$ dB
Maximum value of the phase filtering error (Kaplan, 1996)	$\sigma_{\varphi, \max} = 15^\circ$
Receiver thermal noise power under $T=290$ K° (Kaplan, 1996)	$N = -204$ dBW

**Table 4.** The characteristics of the navigation receiver performance

The maximum allowable phase filtering error value  $\sigma_{\varphi, \max} = 15^\circ$  is determined with Monte Carlo simulation of GPS receiver phase lock loop performance under the combined dynamic and signal-to-noise ratio conditions (Kaplan, 1996). Considering the characteristics in Table 4 and using Eq. (13), we have determined the minimum allowable signal-to-noise ratio at the receiver input,  $CN_{thr}$  for frequencies L1 and L2 of GPS and GLONASS. In the case under consideration,

the  $CN_{thr}$  values of GPS and GLONASS turned out to be very close to each other: 24.59 dB and 24.56 dB for L1 and L2, respectively.

The values of unjammed  $CN_o$  ratio were computed with Eq. (.16), taking in account that  $T_o = 290K$ ,  $N_f = 4$  dB,  $L = 2$  dB (Kaplan, 1996) and  $G(\theta) = -2$  dB ( $\theta > 15^\circ$ , Table 1). Corresponding values of equivalent signal-to-noise ratio at the receiver input  $CN_{eq}$  under the direct influence of solar radio emission (14) are calculated using data of solar radio emission power (Table 3), which are transformed into a jam-to-noise ratio in terms of dBW ( $J/S$  in the equation 14).

Fig. 2 presents results of these calculations for L1 and L2 signals of GPS and GLONASS. The horizontal solid lines in all figures show the minimum allowable signal-to-noise ratio at the receiver input  $CN_{thr}$  and the horizontal dotted and dash-dotted lines stand for unjammed  $CN_o$  values for CA (SP) code (pink lines), P(Y) or the HP code at frequency L1 (blue lines) and for P(Y) or the HP code at frequency L2 (black lines), respectively. The other curves show the  $CN_{eq}$  values for the CA (SP) code (pink curves), P(Y) or the HP code at frequency L1 (blue dotted curves) and P(Y) or the HP code at frequency L2 (black dashed curves).

Three cases were considered:

1. the ranging code on the receiving side is well known, and there are no correlation losses (Fig. 2a,b);
2. "semicodeless" (Fig. 2c, d) and "codeless" processing (Fig. 2e, f) for signal extraction with using unknown code.

From Fig. 2 we can conclude that the signal of C/A (SP) code at L1 frequency turns out to be the most resistant to the influence of the solar radio emission. The equivalent signal-to-noise ratio for the SP signal (GLONASS) in the case under consideration is higher than the  $CN_{thr}$  critical level, even under the influence of the solar radio emission flux of  $10^6$  sfu (Fig. 2a and b). At the same time, the  $CN_{eq}$  value for the C/A signal (GPS) reduces more noticeably and can drop below  $CN_{thr}$  level when solar radio noise power is just about  $10^6$  sfu (Fig. 2a). Thus we can expect the failure in the C/A signal tracking when the power level of solar radio noises is  $\approx 10^6$  sfu. In our opinion this conclusion can be explained with the idea that the front-end pass-band of the GPS receiver radio path is wider than that one of GLONASS receiver particular satellite radio channels. Hence, integral power of the solar radio noise which penetrates into a GPS receiver is higher in comparison to the GLONASS one.

When high-precision ranging codes (P(Y) and HP) on the receiving side are known, stable tracking of these signal components in GPS and GLONASS receivers is provided with a high quality even under the influence of solar radio noises of more than  $10^6$  sfu (Fig. 2a and b). However signal tracking of these components can fail when the power level of solar radio emission is more than 38.000 sfu (the P(Y) component at frequency L2, Fig. 2c) when the "semicodeless" correlation processing is used. Since the power of P(Y) and HP signal components at frequency L1 is considerably higher, the tracking of these components may fail when the rate of the solar radio emission flux is more than 100.000 sfu (Fig. 2c and d).

The situation is the worst when the "codeless" processing of encrypted signals is utilized (Fig. 2e and f). One can see that the P(Y) signal tracking fails when the solar radio noise powers are

about 4000 sfu and 10.000 sfu at frequencies L2 and L1, respectively. The corresponding power levels of the solar radio emission flux that can cause the failure of the GLONASS high precision signal tracking at frequencies L1 and L2 are 10.000 and 13.500 SFU, respectively.

Note that these estimations have been obtained for relatively favorable initial conditions, assuming relatively good Allan deviation factor and no dynamic stress or vibrations. We have also ignored effects of amplitude and phase ionospheric scintillations, which may cause significant fading of signal amplitude at the receiver antenna output. The multipath-propagation effect of signals in the reception point has also been ignored. Nevertheless, we have obviously proven the negative effect of powerful solar radio emission on the GPS and GLONASS performance.

### 2.3. Experimental statistics of GPS phase slips and counts omission during powerful solar flares

We use GLOBDET software developed at the ISTP SB RAS to process GPS data from the global network of dual-frequency receivers (Afraimovich, 2000). For analysis we used data in RINEX (Gurtner and Estey, 2009) format. We collected data over 1500 GPS sites from IGS network (<http://sopac.ucsd.edu/other/services.html>). For December 6, 2006 we used RINEX files from the CORS network (262 sites at <ftp://www.ngs.noaa.gov/cors/rinex/>). We also employ data from the Japanese GPS network GEONET (about 1225 stations) for December 13, 2006.

Fig. 3 shows the experimental geometry of GPS measurements during the solar flare on December 6 and 13, 2006. The GPS sites are marked by dots. Stars indicate the location of sunlit points for the solar flare on December 6 and 13, 2006. We calculate the 30 s series of the L1-L2 phase difference on two GPS frequencies  $f_1$  and  $f_2$  along lines of sight (LOS) of "receiver-satellite" to confirm a slip in measurements of the L1-L2 phase difference (Afraimovich et al., 2002). These data for each GPS satellite are then averaged over a period of  $dT=5$  min at all chosen sites. It allows us to calculate the average number of observations  $S(t)$  and slips  $N(t)$  for all  $n$  LOS. Further we calculate the average relative density of slips  $P(t) = 100\% \cdot N(t)/S(t)$ , and determine the maximal value  $P_{max}$ . If some count in a RINEX file is absent, the number of slips is equated to that of expected observations, so the density of slips becomes equal to 100 %.

Failures in L1-L2 make precision positioning in the dual-frequency mode impossible. The positioning is generally impossible if the signal at both GPS operating frequencies is not received at all. In order to estimate a probability of such failures for all LOS we define a number of counts omission  $M(t)$  for each 30 s observation epoch. Considering  $S(t)$  as an expected number of observation within the current epoch, we define counts omission density as  $W(t) = M(t)/S(t)$ . we also determine the corresponding maximum value  $W_{max}$ . The 30 s time resolution of the  $W(t)$  rows allows us to conduct a detailed analysis of time behavior of  $W(t)$  values under the solar radio emission flux variations.

In order to compare GPS and GLONASS noise immunity, we compute the relative losses-of-lock density  $Q(t)$  in percent of the main signal parameters: L1, L2 (signal carrier phase), and C1, P1, P2 (C/A (SP) and P(Y)(HP) code delay) at  $f_1$  and  $f_2$  GPS and GLONASS frequencies. a

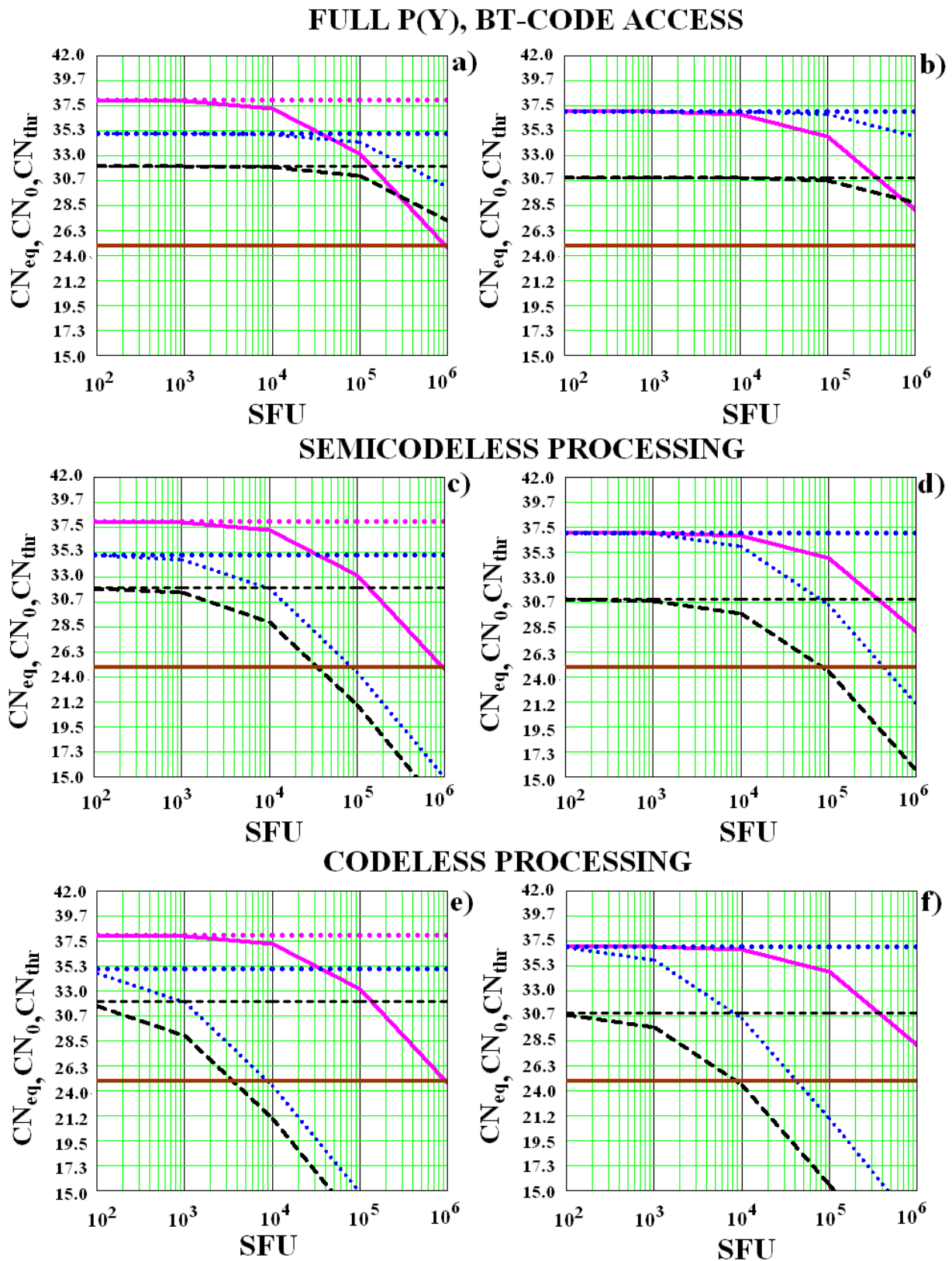


**Figure 2.** An equivalent signal-to-noise ratio for GPS (a, c, e) and GLONASS (b, d, f) navigation receiver input under direct influence of the solar radio emission in units of sfu

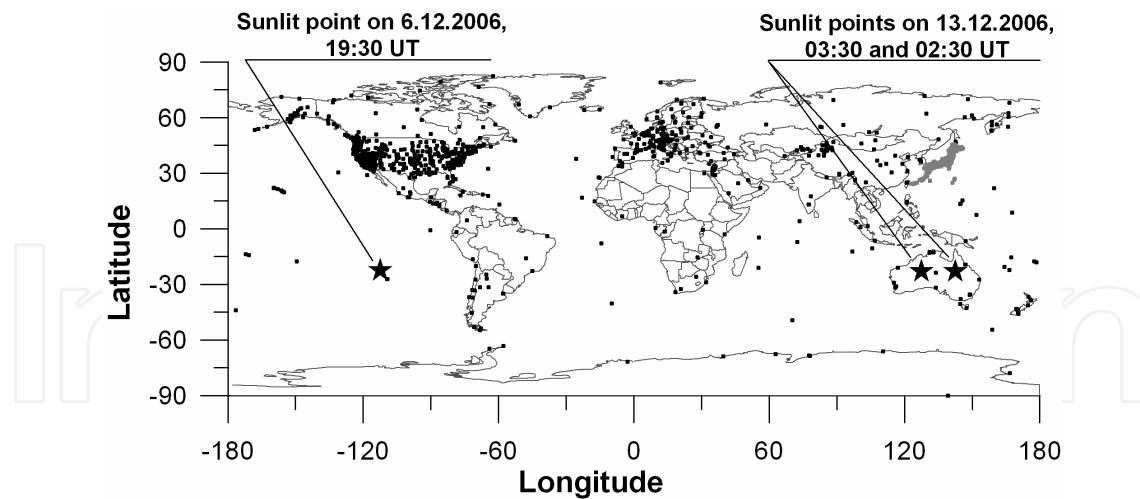


**Figure 3.** GPS measurement geometry during the solar flare on December 6 and 13, 2006. The GPS sites are marked by dots. Asterisks show the location of sunlit points for the solar flare

measurement slip is an event when the current epoch count of corresponding GPS parameters equals to zero or this count was absent in the RINEX file.

Unfortunately, there on December 6 and 13, 2006 there were only 44 combined GPS/GLONASS sites available. Using these data we were able to investigate GPS measurement slips in more details. We utilized the combined GPS/GLONASS data set to conduct the comparative analysis of GPS and GLONASS noise immunity under the direct solar radio emission interference. Due to uneven distribution of GPS/GLONASS sites on the earth surface there were only 4 and 7 sites within the sunlit side of the earth on December 6 and 13, respectively.

#### 2.4. GPS phase slips and counts omission as a result of solar radio bursts on December 6, 2006

According to the data from the Owens Valley Solar Array (OVSA), the power of solar radio emission on December 6, 2006 in the GPS frequency band exceeded  $10^6$  sfu. The background emission level is about  $\sim 10\text{--}10^2$  sfu. Fig. 4e shows the right handed circular polarization (RHCP) radio emission spectrum at 1.2–2.0 GHz, registered at the Solar Radio Spectrograph OVSA. The planetary index of geomagnetic activity was  $K_p \sim 4$ .

Fig. 4a presents the  $P(t)$  time dependences on the earth sunlit side ( $200\text{--}300^\circ$  E;  $-80\text{--}80^\circ$  N). these  $P(t)$  data were derived from  $n=12793$  LOS observations for all observable GPS satellites which were recognized with their pseudo random noise (PRN) code numbers at the elevation  $\theta > 10^\circ$  during the observation time from 18:00 to 20:00 UT (heavy black line). Fig. 4a shows significant increasing of the  $P(t)$  within 19:30–19:40 UT above the background level of slips, which usually does not exceed  $P_{max} \sim 0.2\text{--}0.3\%$  for such weakly disturbed ionosphere (Afraimovich et al., 2009a). Sharp increases of  $P(t)$  values corresponded to an abrupt increasing of the solar radio emission flux at the very period of time.

The maximum relative density value of slips  $P_{max}=18.5\%$  exceeded the background one in about  $\sim 50$  times. At the same time, the average density  $P(t)$  on the earth night side for  $\theta > 10^\circ$  and

$n=3521$  LOS did not exceed the background one. Unfortunately, the time resolution of  $P(t)$  dependence,  $dT=5$  min appeared to be insufficient to display the fine time structures of the radio emission flux (Fig.4e), obtained with the resolution lower than 1 s.

Nevertheless, the concurrence in the form of envelopes of the phase slip distribution and solar radio flux is obvious. The  $W_{max}$  values, observed from 19:15 to 19:45 UT, can reach 82% and 69% (PRN12,  $n=50$  GPS sites; and PRN24,  $n=299$  GPS sites). It can be seen from Fig. 4b that the sharp increase in phase slips and number of counts omission is totally consistent with the moments of the most powerful solar radio bursts (moments T1, T2, T3). Deep fading of the signal-to noise ratio at the L1 GPS frequency was observed during the same periods of time. It proves the idea that such sharp fading of GPS signal-to noise ratio is caused by direct interference of solar radio emission in the 1-2 GHz frequency band.

## 2.5. GPS phase slips and counts omission as a result of solar radio bursts on December 13, 2006

According to the data from the Learmonth Solar Radio Spectrographs, the total flux  $F(t)$  of radio emission on December 13, 2006 exceeded  $10^5$  sfu at 1415 MHz (Fig. 5e). Sharp increasing of the solar radio flux power can be noted within the time periods 02:20 to 02:28 UT (time interval A) and 03:30 to 03:37 UT (time interval B). The horizontal line marks the spectrograph amplitude saturation level of about  $\sim 110000$  sfu.

According the data from the Nobeyama Radio Polarimeters ([http://solar.nro.nao.ac.jp/norp/html/event/20061213\\_0247/norp20061213\\_0247.html](http://solar.nro.nao.ac.jp/norp/html/event/20061213_0247/norp20061213_0247.html)), the RHCP solar radio emission power exceeded  $1.47 \cdot 10^5$  sfu at 1 GHz at 02:28:09 UT and  $2.57 \cdot 10^5$  sfu at 2 GHz at 03:35:51 UT on December 13, 2006. Since there were too few GPS sites on the earth sunlit side (40-200 E; -80+80 N) on December 13, 2006 (<http://sopac.ucsd.edu/other/services.html/>) we used the data set from the Japanese network GEONET which comprises 1225 GPS permanent sites. Fig. 5a, b shows the dependences  $P(t)$  for the December 13, 2006 flare over Japan for some satellites which were observed from 02:15 to 03:45 UT. Maximum values  $W_{max}$  can run to 50% (PRN13) and 27% (PRN16). The sharp increase of count omissions coincide with the impulses of solar radio emission during the time intervals A and B.

For the December 13 flare, on the earth sunlit side (40°-200° E; -80°+80° N) Fig. 5c and d present  $W(t)$  values of counts omission which were registered for all satellites observed from 02:15 to 03:45 UT. Obviously, the maximum values  $W_{max}$  can reach 50% and 39% (PRN28,  $n=16$  GPS sites; and PRN08,  $n=23$  GPS sites). It has shown that the sharp increase of slips and count omissions completely coincide with the impulse solar radio bursts during A and B periods, including the fine time structure of solar radio burst.

## 2.6. GPS phase slips and counts omission as a result of solar radio bursts on October 28, 2003

it is especially interesting to assess GPS measurement slips density caused by the weaker solar radio burst on October 28, 2003. the power of this burst was by 3 orders of magnitude less than the solar radio bursts on December 6 and 13, 2006.

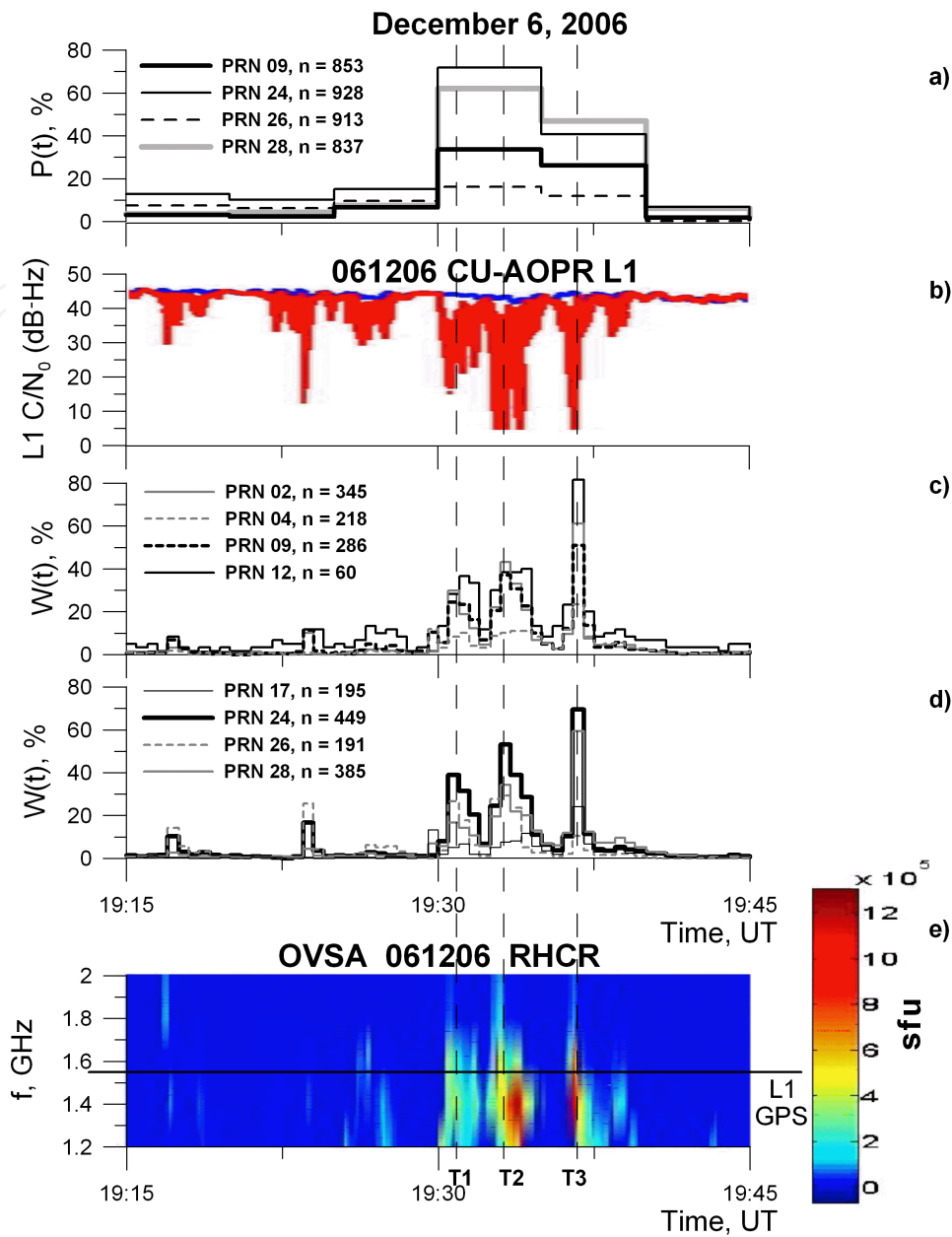


**Figure 4.** GPS L1-L2 phase slips on December 6, 2006

According to the data from the Trieste Solar Radio Spectrograph, Italy, the RHCP solar radio noise level exceeded  $3 \times 10^3$  sfu at 1420 MHz on October 28, 2003 (Fig.6e). There are two solar radio bursts when the power of radio emission flux exceeded the level of  $3 \times 10^3$  sfu: within the time periods from 11:05 to 11:08 UT (time interval A) and from 11:40 to 12:00 UT (time interval B).

Fig. 6d (black line) presents  $P(t)$  dependences for the October 28, 2003 flare on the earth sunlit side ( $330-120^\circ$  E;  $-80+80^\circ$  N) derived from  $n=2452$  LOS observations, for all observable satellites at the elevation angle  $\Theta > 10^\circ$  during the time period from 11:00 to 12:00 UT. A significant excess of the background level,  $P_{max} \sim 0.2-0.5$  %, was observed from 11:02 to 11:10 UT. This

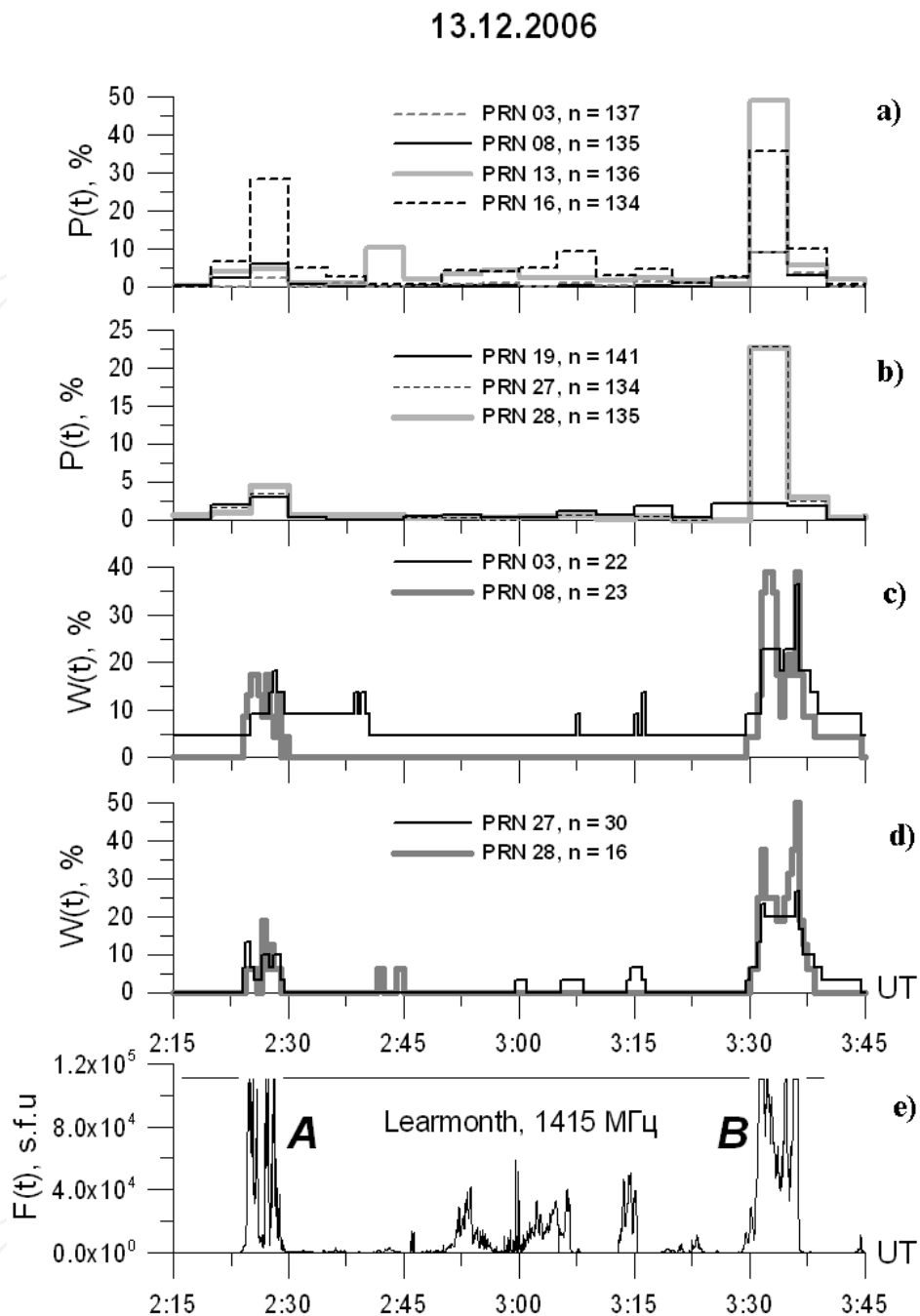


**Figure 5.** GPS L1-L2 phase slips on December 13, 2006

event corresponds to an abrupt increase of the solar radio emission flux during time interval A. The maximum value  $P_{max}=1.7\%$  exceeds the background one in about ~3-4 times. At the same time, the average density of slips on the night side of the earth for  $\Theta > 10^\circ$  ( $n=12070$  LOS) does not exceed the background one (Fig. 6d, thin gray line).

more substantial evidence on GPS-functioning quality deterioration can be found by estimating the average relative density of slips for separate GPS satellites. In Fig. 6a-c, the  $P(t)$

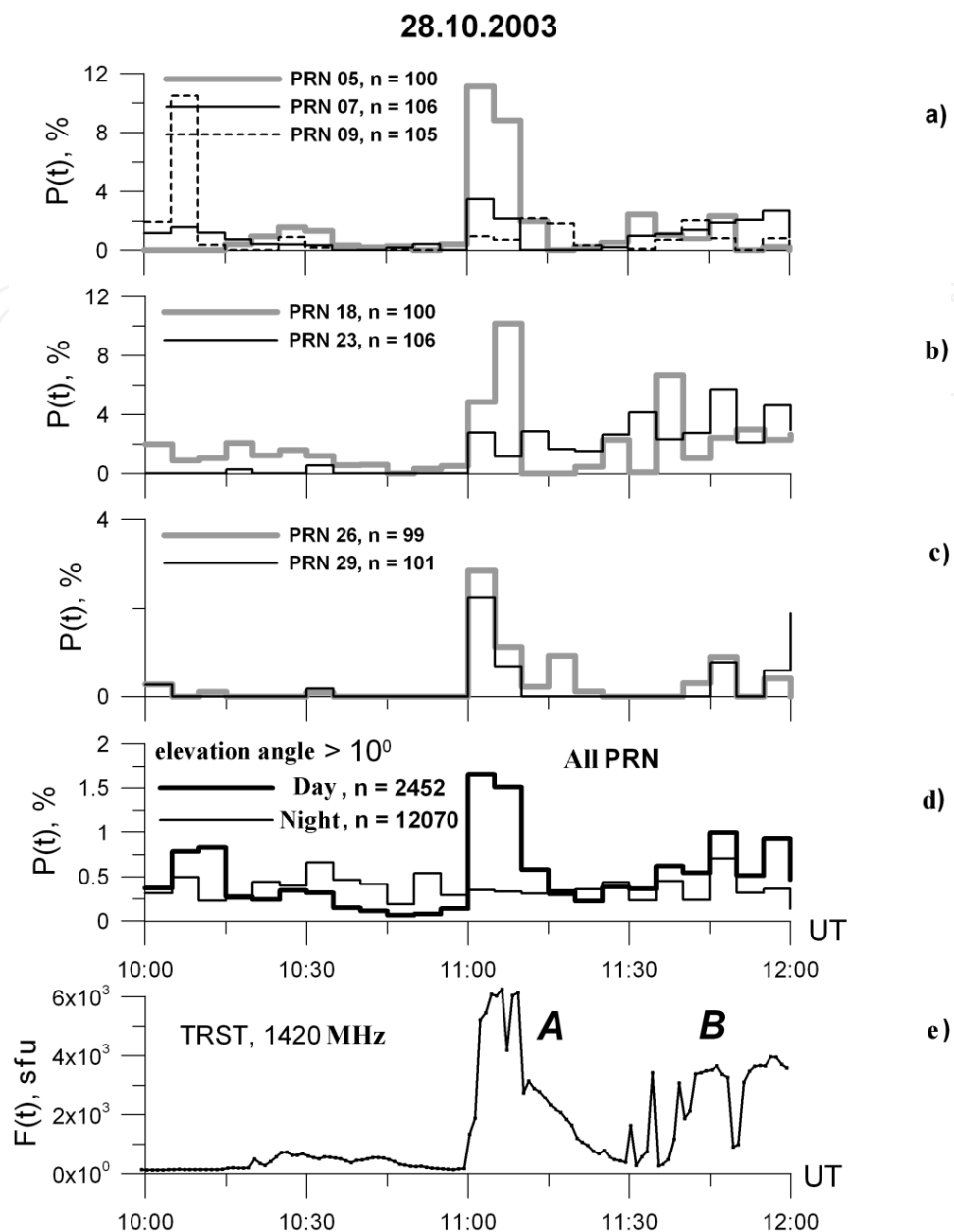


**Figure 6.** GPS L1-L2 phase slips on October 28, 2003

dependences are given for some satellites observed during the time period 10:00 to 12:00 UT. The maximum values  $P_{max}$  can reach 11% and 10.2 % (for PRN05 and PRN18,  $n=100$ ), whereas the value  $P_{max} = 2.3$  % for satellite PRN29 is close to  $P_{max} = 1.7$  %, which was determined for all satellites. The sharp increasing of slips density and count omissions happened simultaneously with the most powerful solar radio bursts for the time intervals A and B. Though power of the solar radio burst on October 28, 2003 is by 2–3 orders of magnitude less than that on December 6 and 13, 2006, the maximum values of phase slips are smaller by only in 5–10 times. Unfortunately the combined GPS/GLONASS data set was not enough in order to analyze the solar radio burst effect on October 28, 2003.

## 2.7. Comparative analysis of GPS and GLONASS performance

It is known that the basic principles of GLONASS and GPS functioning are almost identical from the viewpoint of estimation of the signal power. Hence, a comparative analysis of the GPS and GLONASS receiver noise immunity under direct interference of the solar radio emission is of obvious interest. For example, in the case of GLONASS, the normalized minimum power should not be less than  $-157$  dBW at the main operating frequency of GLONASS (1600 MHz) and  $-163$  dBW at the auxiliary frequency 1250 MHz (ICD-GLONASS, 2002). The corresponding standard for GPS determines these values as  $-163$  dBW at the main frequency of GPS (1545.42 MHz) and  $-166$  dBW at the second operating frequency (1227.6 MHz) (ICD-GPS-200c, 1993).

As we can conclude from the Fig. 1 signal-to-noise ratio at GLONASS receiver antenna output is 7 dB lower than the GPS one under the same solar radio emission power. It seems that we should expect lower noise immunity for GLONASS receivers under the same level of solar radio emission interference. Nevertheless, Fig. 2 convincingly proves that GLONASS noise immunity should be higher. Our experimental results confirm that GPS receivers presented lower noise immunity under solar radio bursts interference on December 6 and 13, 2006.

Fig. 7 presents relative densities  $Q(t)$  of L1, C1, L2, P1, and P2 measurement failures respectively, which were computed for all observed GPS satellites (thick gray curves) and GLONASS satellites (thin black curves) registered within the sunlit zone on December 6 and 13, 2006. Symbols A (December 6) and B (December 13) mark the time intervals when the maximal level of solar radio emission power was  $>10^6$  sfu (December 6) and  $>10^5$  sfu (December 13), respectively. As one can see, there is high reliability of L1 and C1 measurements on the main operating frequency of both GPS and GLONASS systems even in the periods "A" and "B" (Fig. 7a,e). No failures of L1 and C1 parameter were detected on December 6 (Fig. 7a). Only coincident short failures of L1 and C1 measurements were found simultaneously for both GPS and GLONASS at 03:34 UT (Fig. 7e). The results are in good agreement with the idea that if we know the ranging code structure exactly we do not have correlation losses and the unsafe level of solar radio emission is about  $10^6$  sfu for both GPS and GLONASS.

The situation is much worse when we utilize the codeless method in order to extract the P(Y) or HP code, in which case we have correlation losses is about  $\sim 27$  dB. We can see sharply increasing  $Q(t)$  values by up to 35% on December 6, 2006 in P1, P2 and L2 parameters of GPS in the very period of sharply increasing solar radio emission power (Fig. 7b,c and d). The situation turned out to be more dramatic on December 13, 2006. One can see the  $Q(t)$  values of P1, P2 and L2 parameters exceed 50% within periods "A" and "B" (Fig 7f,g and h).

More important result consists of the fact that the maximum  $Q(t)$  value of all signal parameters of GLONASS, except for L1 and C1, is lower than the one for GPS by a factor of 2-4. In our opinion this advantage is due to the fact that a GLONASS receiver can perform its function more reliably under conditions of the powerful solar radio interference because of the narrower front-end passband of the GLONASS receiver for the separate GLONASS satellites compared to the GPS receivers. Unfortunately, the small statistics did not allow us to get more statistically significant assessments. We will further investigate it in the near future.

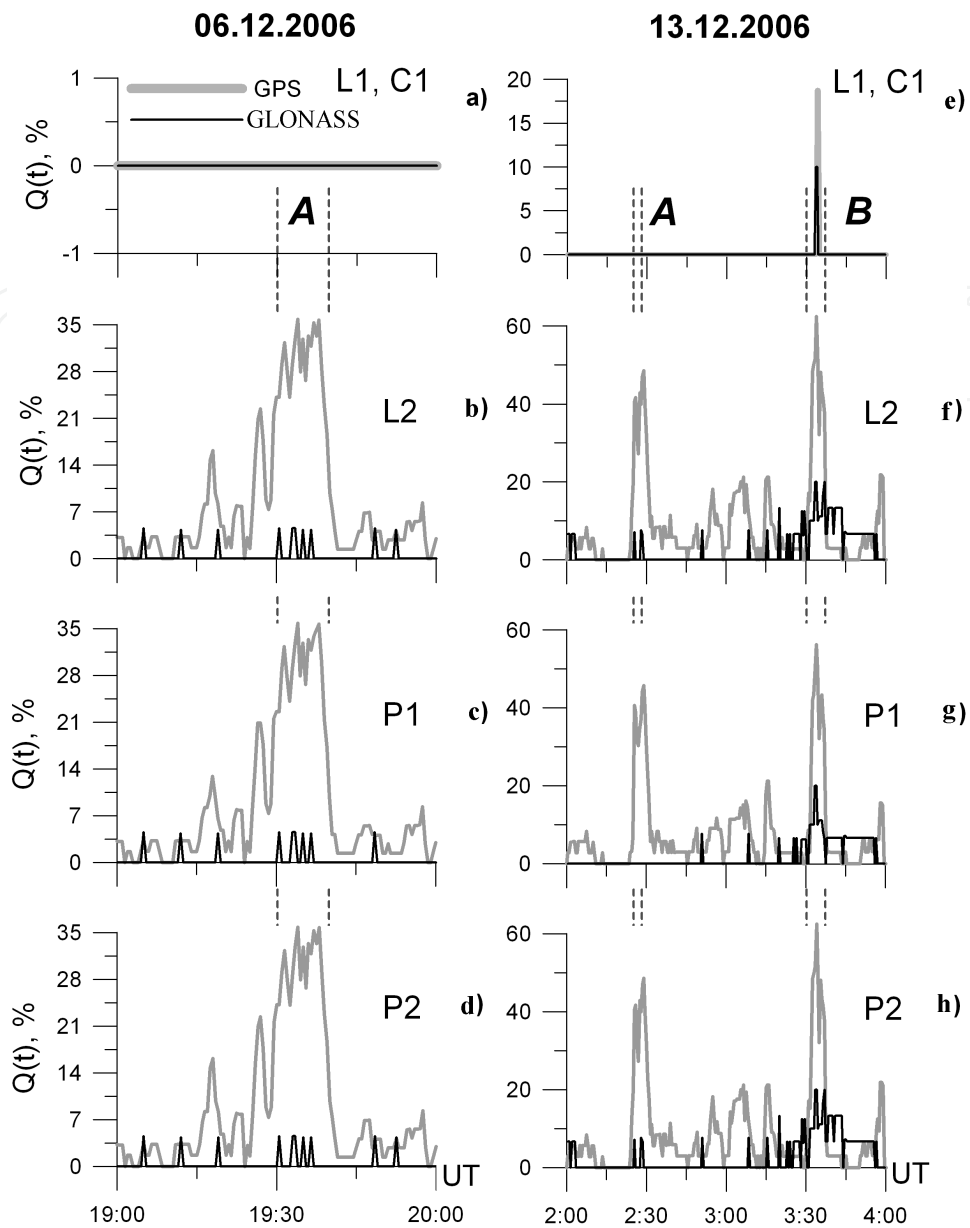


**Figure 7.** A comparative analysis of GPS and GLONASS noise immunity under powerful solar radio emission interference on December 6 and 13, 2006

As the whole results in Fig. 7 prove our theoretical assessments of the unsafe level of solar radio emission when GPS (GLONASS) signal tracking failures appear. The comparison between global failures of the GPS and GLONASS shows that the unsafe level of solar radio emission for GLONASS is higher than GPS. Thus, we have obtained the “unsafe” power level of the solar radio emission that could cause failures of GPS and GLONASS signal tracking. It was found that signal tracking started to fail when the solar radio emission power is about 4000 sfu at the GPS frequency L2 and 10.000 sfu at the frequency L1 when the “codeless” correlation processing technique is utilized. These assessments for GLONASS turned out to be 10.000 and 13.500 sfu at frequencies L1 and L2, respectively. Hence the GLONASS naviga-

tion receivers are more resistant to intensive solar radio emission under considered conditions. In our opinion this occurs because the GLONASS receiver radio path is characterized with a narrower front-end passband in order to provide effective extraction of signals of the particular GLONASS satellites.

Our theoretical assessments are proven by experimental statistics of GPS phase slips and counts omission that was found during powerful solar flares condition on December 6 and 13, 2006 and, especially, during the much weaker solar radio burst condition on October 28, 2003. It is very important to emphasize that although power of the solar radio burst on October 28, 2003 is by 2–3 orders of magnitude less than that on December 6 and 13, 2006, the maximum values of phase slips are only 5–10 times less. Particular slips of L1-L2 phase measurements started to appear under the interference of solar radio flux when power was just a bit higher than  $10^3$  sfu.

Experimental results have shown that for over 10–15 minutes the high-precision GPS positioning was partially disrupted on all sunlit sides of the earth on December 6 and 13, 2006. The high level of phase slips and count omissions resulted from the wideband solar radio noise emission. The statistics of phase slips obtained in this study for all sunlit sides of the earth confirms the suppression effect of GPS receiver performance during the December 6, 2006 flare with more reliability than the previously published, which were obtained and discussed at only several GPS sites by Carrano et al. (2007) and Cerruti et al. (2006).

In general, our results are in good agreement with earlier results by other authors, which indicate that direct impact of the solar radio emission can cause failure in GPS signal tracking of navigation receivers, even if the solar radio emission power is relatively low (about  $10^3$  sfu). It proves that solar radio noises of more than  $10^3$  sfu can have a negative influence on the GPS/GLONASS performance.

### **3. Ionospheric super-bubble effects on GPS performance**

Strong scintillations of amplitude and phase of transionospheric radio signals occur due to signal scattering on intensive small scale irregularities (Yeh and Liu, 1982). The size of such irregularities is the order of the first Fresnel zone radius, 150-300 m for 1.2-1.5 GHz frequency band. Scintillation can have an adverse effect on GPS signals and cause a GPS receiver to lose of signal lock in some extreme cases. Positioning quality deterioration can appear as a direct consequence of such physical phenomenon.

Over recent years, extensive studies of mid-latitude GPS phase fluctuations and phase slips under geomagnetic disturbances condition have been made (Skone, 2001; Conker et al., 2003; Ledvina et al., 2002, 2004; Ledvina and Makela, 2005; Afraimovich et al., 2002, 2003, 2009b; Astafyeva et al., 2008; Meggs et al., 2006). The expansion of the auroral oval equatorward is known to be accompanied by an increase of a number of slips in satellite signal tracking and GPS positioning deterioration in the mid-latitude region (Afraimovich et al., 2002, 2003, 2009b).

Ionospheric irregularities and steep gradients often occur at high-latitude ionosphere which is strongly disturbed due to auroral substorms. Existence of the ionization anomaly at low-latitudes, along with the well-known effect of the equatorial plasma bubble formation during the evening hours, increases the possibility for transionospheric signal fading in this region as well. Though the mid-latitudes are considered comparatively quiet, strong perturbations of plasma density are often observed at mid-latitudes as well. This is related to expanding either the auroral oval or the equatorial anomaly, especially during geomagnetic storms.

The plasma bubbles are associated with equatorial spread F (ESF) processes. A plasma bubble develops along the Earth's magnetic field line, elongated in the meridional direction, but it is much narrower in the zonal one. The plasma bubble has a finite height, and the poleward limit is determined by its equatorial height. The equatorial bubbles are not often observed at mid-latitudes. Observations have shown that in rare cases the ESF density depletions can reach high altitudes and extend to the equatorial anomaly latitudes. For example, satellite measurements showed that the ESF plasma depletions may reach apex altitude of 2000-6000 km (Burke et al., 1979; Obara and Oya, 1994; Ma and Maruyama, 2006; Huang et al., 2007). Nevertheless, it is not fully understood yet how high ESF bubbles can emerge.

Although the ESF plasma bubble is a common phenomenon and it has been studied for years, precise observed data of ionospheric scintillations and loss of lock to GPS receivers at mid-latitude due to plasma bubbles affectation are still limited. A post sunset bubble manifested by loss of L2 signal lock was observed at mid-latitudes ( $\sim 30^\circ\text{-}34^\circ\text{N}$ ,  $\sim 130^\circ\text{-}134^\circ\text{E}$ ) during the main phase of the 12 Feb 2000 storm (Ma and Maruyama, 2006). The bubble had unusually large latitudinal extension reaching mid-latitude of  $36.5^\circ\text{N}$  ( $31.5^\circ\text{N}$  magnetic latitude), indicating an apex height of  $\sim 2500$  km.

However, in most papers there are no data regarding the space geometry of field-aligned irregularities (FAIs). For example, Ma and Maruyama (2006) have identified their observations as bubbles using only the following criteria: the occurrence time (post sunset), the availability of phase slips, the total electron content (TEC) and DMSP local density depletion. But the above criteria are insufficient to identify the bubbles. It is necessary to obtain some direct evidence of the obliqueness of the scattering structure (i.e. FAI) along the magnetic field line.

What is the physical nature of the above phenomenon? It is necessary to obtain some direct evidence of the obliqueness of the scattering structure along the magnetic field line. We propose to use the additional information regarding angular characteristics of the scattering process. Our main idea was to test the relation between the LOS direction  $r$  and the direction of magnetic field line vector  $\vec{B}$  at the altitude  $h_{max}$  of the ionospheric F2 layer maximum where the intensive irregularities causing the scattering of GPS signals and losses of L1 and L2 phase lock are located.

The goal of Section 3 is to describe our method of GPS detecting the mid-latitude FAIs, using loss of L2 phase lock, and to estimate their characteristics by example of the unusual February 12, 2000 events. Furthermore, it will further analyze the dependency of GPS positioning quality on the orientation of signal propagation relative to geomagnetic field lines during the regis-

tered super-bubble on February 12, 2000 on the basis of from the Japanese GPS network GEONET.

### 3.1. Mid-latitude field-aligned irregularities from GPS

Ma and Marayama (2006) have used only 300 GPS receivers selected homogeneously from GEONET to analyze loss of L2 signal lock for each visible satellite. We carried out our analysis for the total number of GPS GEONET receivers (~ 1000). We determine the azimuth  $\alpha_s$  and the elevation  $\theta_s$  of the LOS between a GPS site and a satellite and analyze L2 phase losses-of-lock density.

We use the data regarding L2 phase losses-of-lock only as initial. The lower signal to noise ratio at L2 is generally due to the fact that the L2 power at the GPS satellite transmitter output is 6 dB less than the fundamental frequency f1 with the C/A code (ICD-GPS-200c, 1993). Phase loss-of-lock at L2 may also be caused by a lower signal to noise ratio (SNR) at L2 frequency when commercial semi-codeless or codeless receivers are used. These receivers have no access to the military «Y» code at L2 GPS frequency. Hence they have to use a specific processing technique in order to extract L2 phase and ranging measurements. As a result we get significant correlation losses and the SNR at L2 is 13-17 dB lower in compare to the full code access mode at least. Thus the loss of signal lock at L2 may be considered as a sensitive indicator of the transionospheric signal scintillations for all kinds of GPS receivers on the global scale under geomagnetic storm conditions (Afraimovich et al., 2002, 2003, 2009b). Such data may be an important addition to the data obtained by a few specialized monitors of ionospheric scintillations in the L range at mid-latitude as well (Kintner and Ledvina, 2005).

On the first step, we determine the coordinates of the ionospheric pierce point  $S_i$  at an altitude of F2 maximum  $h_{max}$  in the geodetic coordinate system  $(\phi_p, \ell_p)$

$$\begin{aligned} \varphi_p &= \arcsin(\sin \varphi_B \cos \psi_p + \cos \varphi_B \sin \psi_p \cos \alpha_s) \\ \ell_p &= \ell_B + \arcsin(\sin \psi_p \sin \alpha_s \sec \varphi_p) \\ \psi_p &= \frac{\pi}{2} - \theta_s - \arcsin\left(\frac{R_z}{R_z + h_{max}} \cos \theta_s\right) \end{aligned} \tag{17}$$

Where  $R_z$  is the Earth radius;  $(\phi_B, \ell_B)$  are GPS site' geodetic coordinates (latitude and longitude),  $(\phi_p, \ell_p)$  are the geodetic coordinates of ionospheric pierce point. Ionospheric pierce point corresponds to altitude  $h_{max} = 300$  km.

Fig. 8 presents our scheme of the LOS angular scanning. The axes  $h$ ,  $Y$ , and  $X$  are directed, respectively, zenithward, southward ( $Y$ ) and eastward ( $X$ ). The arrows  $LOS$  indicate the direction  $\vec{r}$  along LOS and the magnetic field line direction  $\vec{B}$ ;  $\theta_s$  and  $\theta_B$  - the elevations of vectors  $\vec{r}$  and  $\vec{B}$ , respectively;  $\gamma$  - the angle between the vectors  $\vec{B}$  and  $\vec{r}$ .  $L_{II}$  and  $L$  are the longitudinal and cross size of large scale bubble, elongate along magnetic field line and containing the set of small scale irregularities. The LOS1 direction (magnetic normal) corre-

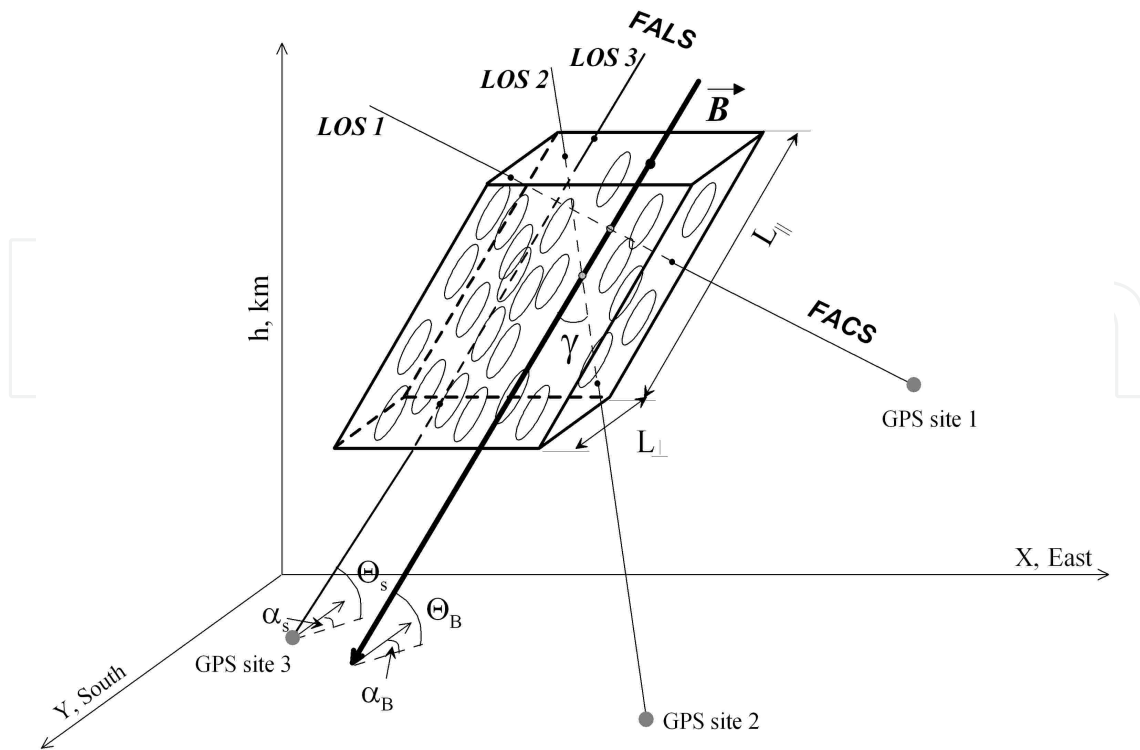


**Figure 8.** The scheme of the LOS angular scanning

sponds to the field of across scattering, F ACS ( $\gamma \sim 90^\circ$ ) and LOS3 direction (magnetic zenith) is near the field of aligned scattering, FALS ( $\gamma \sim 0^\circ$ ).

We calculate magnetic field line direction at altitude  $h_{max}$  in the ionospheric precise point  $S_i$  using the International Geomagnetic Reference Field model IGRF-10 (<http://ngdc.noaa.gov/IAGA/vmod/igrf.html>) and determine the angle  $\gamma$  between the vectors  $\vec{r}$  and  $\vec{B}$ . Then we calculate the histograms  $N(\gamma)$  of number of L2 phase losses-of-lock on the dependence of the angle  $\gamma$  value. The angular histogram bin  $\Delta\gamma$  equals to 1 degree for all our results.

Fig. 9 presents the L2 phase losses-of-lock statistics on 12 Feb 2000: In the Fig 9a the map of sub-ionospheric points with the L2 losses-of-lock is presented (11:00-14:00 UT, PRN 7, 20773 30-sec counts, black dots; PRN 13, 25474 counts, gray dots; PRN16, 2758 counts, blue dots; and PRN24, 3175 counts, red dots). Fig. 9b shows the time dependence of the numbers of L2 losses-of-lock  $N(t)$ . The scale for PRN16 is shown on the right. Fig. 9e shows the angular trajectories of the sub-ionosphere points for GEONET GPS site 3054 ( $34.7^\circ\text{N}$ ,  $137.7^\circ\text{E}$ ) during whole day February 12, 2000. The filled circle and filled band mark the LOS angular field near FALS and FACS band, respectively, with angular window of about  $10^\circ$ ; violet curve correspond the  $\gamma = 90^\circ$ . Fig. 9c is the same as Fig. 9e, but for all PRN during whole day 12 February 2000.

One can see the good likeness of Fig. 9a to the Fig. 4 from the paper by Ma and Marayama (2006). But here we can see the detailed distributions of losses of L2 phase lock for selected PRN. The number of L2 phase losses-of-lock  $N(t)$  runs up to unexpectedly high value (up to

230 receivers for PRN 13) in ten minutes (Fig. 9b). The total number of L2 losses-of-lock is very significant; it corresponds to a very high level of scintillations, caused by GPS signal scattering on the intensive small scale irregularities. The effects of GPS signal multipath may be the alternative reason of such a deep radio-signal decay which causes the L2 signal lock.

Fig. 9f (blue line) shows the total histograms  $N(\gamma)$  for all PRN during the whole day February 12, 2000. First of all, the total number of L2 losses-of-lock is very significant ( $\Sigma N = 149948$ ). Furthermore, the greatest number corresponds to the low value of the angle  $\gamma$  and the angle  $\gamma$  near  $90^\circ$ .

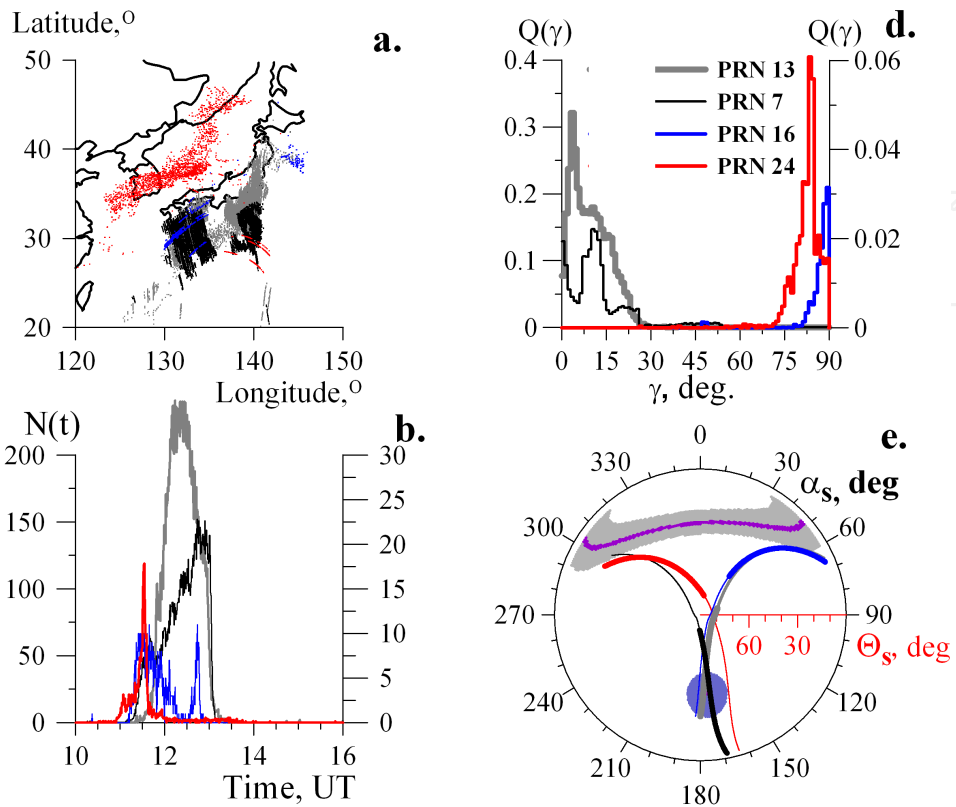
For the adequate angular distribution calculation it is necessary to take into consideration the real distribution of all LOS angular counts, the background function  $S(\gamma)$ . Fig. 9f (black line) gives the total histograms  $S(\gamma)$  for all PRN during whole day February 12, 2000 ( $\Sigma N = 17961082$ ). The most probable value  $S$  equals of about  $64^\circ$ ; the least probable value  $S$  corresponds to the FALS. Fig. 9f presents the procedure of normalization of distribution  $N(\gamma)$ : the blue, black and red lines are the initial series  $N(\gamma)$ , the background function  $S(\gamma)$ , which equal to the total amount of 30-s samples for chosen value of  $\gamma$ , and the normalized distribution  $Q(\gamma) = N(\gamma)/S(\gamma)$ , respectively. One can see that the normalized distribution  $Q(\gamma)$  differs from initial series  $N(\gamma)$  significantly; the most probable value of  $\gamma$  for all L2 phase losses-of-lock during the whole day 12 Feb is close to the FALS.

The Fig. 9d shows the normalized distribution of L2 losses-of-lock  $Q(\gamma)$ . The scale for PRN16 and PRN24 is shown on the right. Let us analyze the time interval 11:00-14:00 in details. Fig. 9d presents the normalized phase losses-of-lock distribution  $P(\gamma)$  of angle  $\gamma$  for chosen satellites (PRN07, PRN13, PRN16, PRN24); the total numbers of L2 phase losses-of-lock are indicated earlier. Corresponding LOS trajectories of the sub-ionosphere points for GPS site 3054 ( $34.7^\circ N$ ,  $137.7^\circ E$ ) are shown in Fig. 9e. One can see that the L2 losses-of-lock are registered near the FALS (PRN 7 and PRN 13) and near the FACS (PRN 16 and PRN 24).

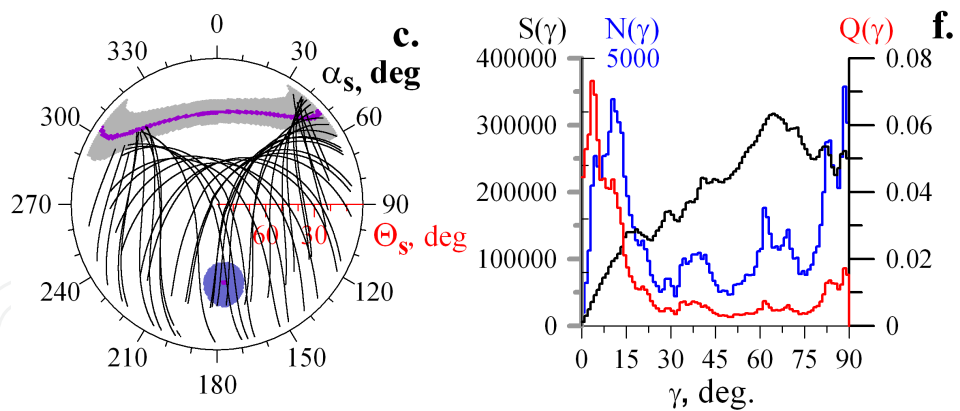
Similar angular dependencies are obtained for other time intervals (05:00-09:00 UT and 16:00-21:00 UT). Above mentioned results confirm well with data of investigation of magnetic field orientation control of GPS occultation observations of equatorial scintillation during detailed LEO CHAMP, SAC-C and PICOSat measurements, realized by Anderson and Strauss (2005). Inclination of LEO orbits allows authors to study magnetic field dependence in wide range of the angle between the occultation ray path and the magnetic field.

Fig. 10 presents the comparison between our the normalized distribution  $P(\gamma)$  of angle  $\gamma$  between the direction  $\vec{r}$  along LOS and the magnetic field line direction  $\vec{B}$  obtained from GEONET data, with the occurrence frequency for occultation events with maximum S4 greater than 0.09 versus the angle between the occultation ray path and the magnetic field from CHAMP and SAC-C measurements (Anderson and Straus, 2005). SAC-C naturally has the largest number of occultation events and greatest probability of occurrence because it orbits half the time within the post-sunset MLT sector where equatorial scintillation is most likely to occur. CHAMP has the smallest because of its lower altitude and the smaller Fresnel scale as discussed earlier. Despite these differences, the data from all three satellites clearly indicate a strong dependence of the occurrence of equatorial scintillation on the angle between the

**February 12, 2000**  
**11:00-14:00 UT**



**All PRN; 00:00-24:00 UT**



**Figure 9.** The statistics of the L2 phase losses-of-lock on 12 February 2000

occultation ray path and the magnetic field. One can see that the maximum values of the S4 occurrence probability and the normalized distribution  $P(\gamma)$  correspond the small values of “B Field/Occultation Angle” and the angle  $\gamma$ . More narrow distribution  $P(\gamma)$  caused by more hard condition for GPS LOS hit in the field of aligned scattering, corresponding to the exact direction of vector  $\vec{B}$ .

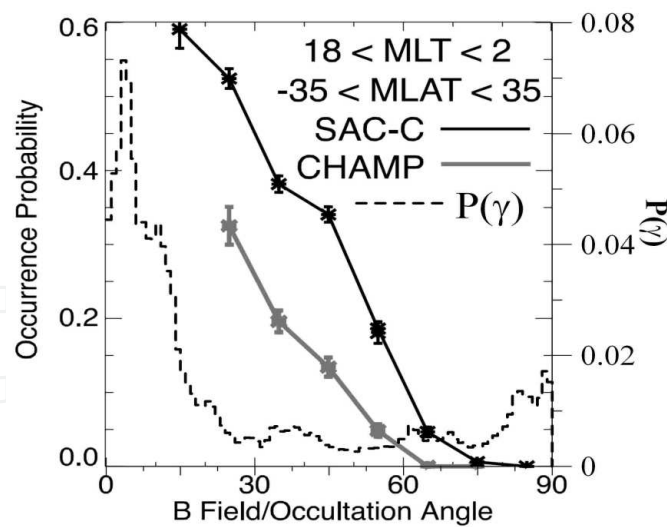


**Figure 10.** Comparison between our normalized distribution  $P(\gamma)$  and the occurrence of maximum S4 from CHAMP measurements (Anderson and Straus, 2005).

We agree with the clear explanation by similar dependence of the occurrence of GPS scintillation on the angle between the occultation ray path and the magnetic field (in our case the angle  $\gamma$ ) presented by Anderson and Straus (2005): “... we must examine the structure of ionospheric bubbles and the instabilities associated with them that lead to scintillation. Bubbles are formed in the bottomside of F region and drift upwards under the influence of horizontal electric fields. The plasma drifts in the post sunset hours are faster near the F peak than at other altitudes, leading to a “C shape” when viewed with imagers from the ground (Woodman and LaHoz, 1976), or from high altitude (Kelley et al., 2003). However, when viewed at a single altitude, the bubbles are nominally stretched out in latitude, or along magnetic field lines (McClure et al., 1977). So the walls of the bubbles are extended vertically upward and stretched in the north-south direction along the magnetic field lines (see Fig.8). Ionospheric interchange instabilities responding to the steep density gradient on the walls of the bubble in the F region produce the electron density irregularities responsible for radiowave scintillation. An occultation with a ray path which is perpendicular to the magnetic field cuts across the bubbles perpendicular to the two walls of the bubble and passes through the regions of density irregularities on the walls only briefly (see Fig. 8). However, an occultation with a ray path that is parallel to the magnetic field may pass along the edge of a bubble and the bubble wall, thus experiencing a path that may remain within the region of density irregularities for a significantly longer period than for occultation events with ray path perpendicular to the magnetic field. Put another way, the “slab thickness” of the irregularity region encountered by the GPS signals is larger when the ray path is aligned more closely to the direction of elongation of the bubble regions. Since scintillation strength increases with irregularity slab thickness (Yeh and Liu, 1982), the observed increase in scintillation occurrence for field-aligned conditions is reasonable”.

The scattering in the field of aligned scattering, was studied well in numerous theoretical investigations and registered earlier many times in equatorial (Kintner et al., 2004) and high

(Wernik et al., 1990; Maurits et al., 2008) latitudes. Our results confirm the main conclusion of these investigations about the control over scintillation by the magnetic field direction. Of special importance are the investigations by Anderson and Straus (2005) where, during radio occultation observations, the scintillation increase at the angle decrease between the ray/LOS and the magnetic field was shown. However, the behavior of scintillations is determined not only by the angle between the field and the ray/LOS (off-B angle; Wernik et al., 1990), but also by some other factors: the elevation angle, the irregularity morphology, etc. This results in emergence of scintillations at large angles between the propagation and the magnetic field (see Fig. 10) which is in good agreement with the observational data, presented by Maurits et al. (2008).

The basic difference of our approach to investigating scintillations is in using of a rather substantial database on the information about malfunctions in the GPS receiving network. As it follows from the above comparison with the direct measurements of scintillations, such an indirect approach with using a close association of scintillations with GPS malfunctions, provides a possibility to monitor scintillations and scintillation-related FAI with an accuracy sufficient enough.

The effect of powerful HF radiation on the ionosphere has been investigated by using signals from high-orbiting GPS/GLONASS satellites (Tereshchenko et al., 2008). For the first time, they detected a quasi-stationary effect of magnetic zenith which leads to a decrease in the electron content and formation of electron density irregularities extended along the magnetic field lines. These authors exhibited the efficiency of GPS/GLONASS satellite signal application to investigate the ionosphere affected by HF radiation. But it is very important to compare the above results with the statistics of background TEC variation and scattering of GPS signals caused by natural field-aligned disturbances.

The scattering peculiarities of the transionospheric signal (when propagating along the magnetic field line) are necessary to take into account in all the radio occultation experiments where inhomogeneous media in the Ionosphere (Anderson and Straus, 2005), solar corona (Hewish and Symons, 1969; Pätzold et al., 1975), planets (Zhuk, 1980) and interstellar medium are investigated (Manchester and Taylor, 1977).

Our results are important for ionospheric irregularity physics development and the transionospheric radio wave propagation modeling. They are especially important in connection with the approaching of solar maximum which will produce strong ionospheric storms, increasing of the background ionization level and level of ionosphere plasma irregularities (Kintner et al., 2009). spatial-temporal features and modeling of mid-latitude FAIs are the goals of our future investigations.

### **3.2. GPS positioning errors during occurrence of a super-bubble**

Figure 11 shows maps of sub-ionospheric points for those satellites for which L2 phase carrier measurements were experiencing slips during 5 minutes of observations. The points of appearance of GPS phase losses-of-lock indicate the values of angle  $\gamma$  by color. We found that before and after the bubble's observation at 10:00 and 13:45 UT respectively, there occurred

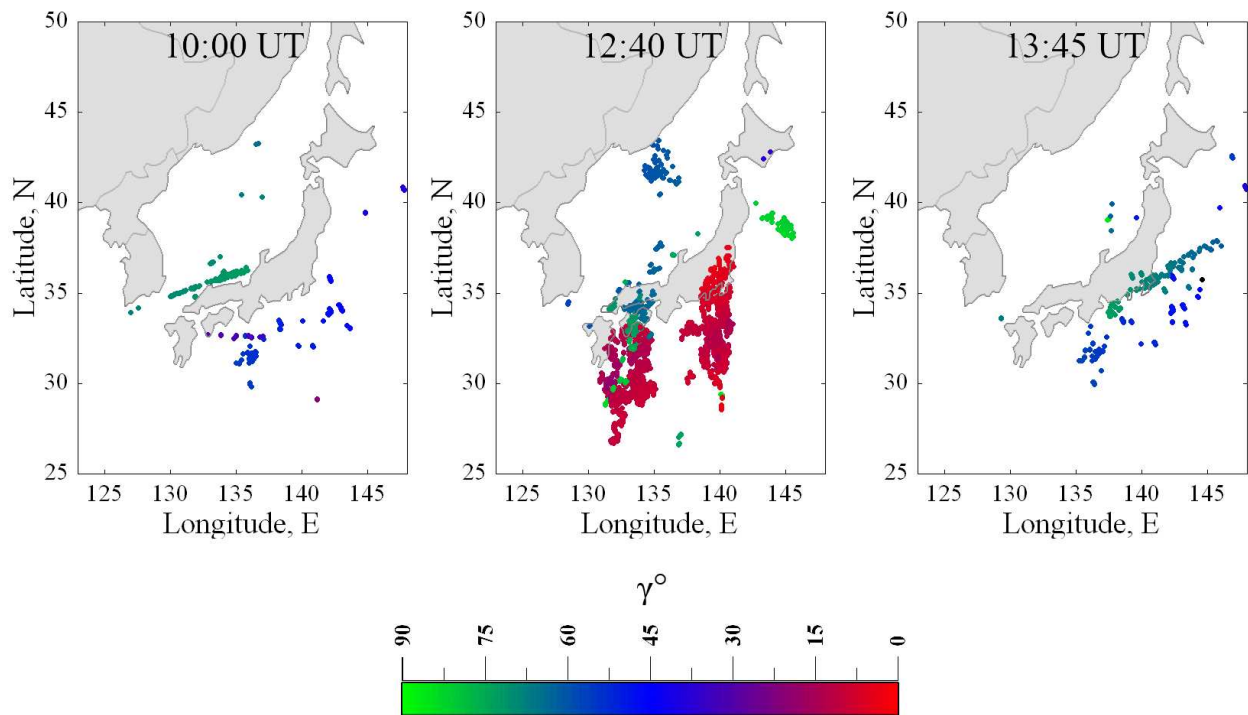


**Figure 11.** Sub-ionospheric points with L2 phase slips. The color scale identifies the size of the angle  $\gamma$ .

few phase losses of phase lock with weakly pronounced dependency on angle  $\gamma$ . The losses-of-lock occurred for the satellites with an angular orientation of LOS for a large range of  $\gamma \approx 35 \dots 80^\circ$ . The situation completely changed by 12:40 UT, when the bubble oriented along the geomagnetic field lines. During this time, we observed significant growth of up to 10 times in the number of L2 phase losses-of-lock. It is important to note that the majority of the observed lock losses corresponded to values  $\gamma \approx 0 \dots 20^\circ$ . In addition, we can see from the figure that these losses were concentrated within two regions, one in the area of evolution and drift of the bubble as was mentioned by Ma and Maruyama (2006), and the other is directed northeastward.

Positioning was carried out by what is called the Navigation Solution epoch by epoch using the dual-frequency ionospheric-free linear combination and the broadcast ephemeris as available from the RINEX files. The positioning errors are then calculated from by

$$\sigma(t_i) = \sqrt{\Delta x_i^2 + \Delta y_i^2 + \Delta z_i^2}, \quad (18)$$

where  $\Delta x_i$ ,  $\Delta y_i$ ,  $\Delta z_i$  are the differences of the estimated geocentric position and the published GEONET coordinates. An event with  $\sigma(t) > 500$  m is considered to represent an instant of a jump in the position estimate.

The distributions of positioning errors calculated for the GEONET stations for 10:00 UT, 12:40 UT and 13:45 UT are depicted in Fig. 12. At 10:00 UT, before the arrival of the bubble, the positioning errors of  $\sigma(t) > 100$  m occurred at 60 GPS receivers, i.e. 6.3% of the GEONET stations.

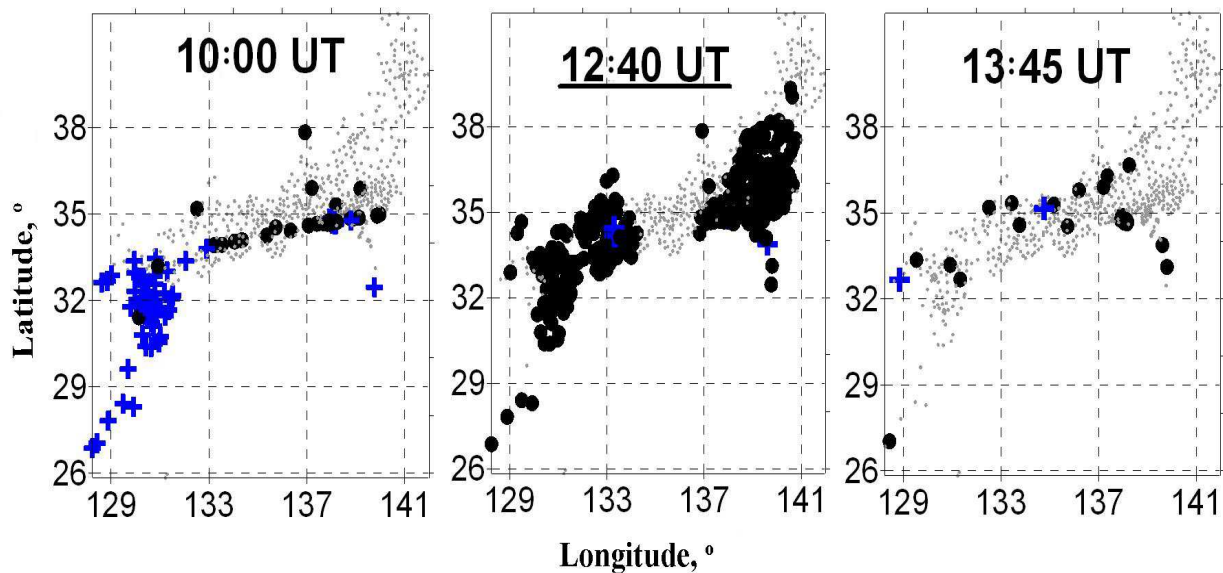


**Figure 12.** Positioning errors and jumps at GEONET GPS stations before the bubble appearance (10:00 UT), during the geomagnetic disturbance maximum (12:40 UT), and after the bubble disappearance (13:45 UT)

For the same time, positioning jumps were observed at 27 stations (2.8% of the stations). Note that the positioning errors mostly occurred on the southwest of the Japanese Islands, while the location of the positioning jumps was more sporadic (Fig. 12, left panel). By the time of the bubble arrived, at 12:40 UT, the number of the positioning errors  $\sigma(t) > 100$  m decreased to 0.4% (4 receivers), whereas the percentage of GPS positioning jumps increased to 33% (313 receivers). Comparison of Fig. 11 and 12 shows that at 12:40 UT the location of the positioning slips coincided with the location of L2 phase losses-of-lock, i.e. the losses-of-lock and jumps were concentrated in the region of the super-bubble. After the disappearance of the bubble by 13:45 UT only 2 GPS receivers (0.2%) registered positioning errors with  $\sigma(t) > 100$  m and 25 stations (2.6%) registered positioning jumps. Note that the jumps occurred mostly in the central part of Japan. Thus, before and after the bubble's appearance, the number of positioning jumps does not exceed 2.6%, whereas during the bubble occurrence that number reaches 33%.

Another important conclusion comes from Fig. 11 and 12. Although the bubbles are not known to propagate farther than  $36.5^\circ$  of latitude (Ma and Maruyama, 2006), their effects on the positioning quality may affect GPS users located more to the north. For instance, we observed occurrence of positioning jumps up to latitude  $38.7^\circ$  (Fig. 12).

In order to further study the relationship between occurrence of positioning jumps and latitude, we analyzed the temporal variations of  $\sigma(t)$  at 12 GPS receivers located in the region of bubble observation. Fig. 13 shows the level of positioning errors between 6 and 16 UT at GPS stations within  $31^\circ$  and  $41^\circ$  latitude. For easy of interpretation of Fig. 13, we set  $\sigma(t) = 0$  whenever a positioning jump was occurred. The figure shows once again that the aspect conditions influence the positioning quality of GPS. From these stations, the northernmost ones (0027, 0024, 0026, bottom panels) did not reveal any indications of the effects of bubbles.

For GPS receivers located below about 38°N numerous positioning jumps occurred between 11-13 UT. This is due to the fact that the bubble did not reach the region of the northern stations.

Thus, using the Japanese GEONET, we observed numerous GPS phase losses-of-lock and positioning errors during the main phase of geomagnetic storm of February 12, 2000. The good coverage of the GEONET made it possible to perform for the first time such a detailed study on spatial-temporal dynamics of radio navigation failures associated with the evolution of electron density irregularities in the equatorial ionosphere.

Numerous GPS L2 phase losses-of-lock occurred during the time of the super-bubble observations from 11 to 13 UT. Moreover, appearance of GPS losses-of-lock was found to depend on the angle  $\gamma$  between the station-satellite LOS and the geomagnetic field lines, with the maximum value of GPS phase losses-of-lock corresponding to  $\gamma=0^\circ$  and  $90^\circ$ . The maximum value of losses in the magnetic zenith region reached 32% and was observed at PRN13. The maximum density of phase losses-of-lock corresponded to the regions with maximum amplitude of TEC variations (and maximum TEC gradients), i.e. the regions of development and drift of the super-bubble as was mentioned by Ma and Maruyama (2006). Before and after the bubble's observations, i.e. before 11:00 and after 13:00 UT, few phase losses-of-lock occurred and their dependency on angle  $\gamma$  was weak.

Analysis of GPS positioning quality showed similar behavior. By the time of the bubble's appearance, 33% of GPS receivers experienced GPS positioning jumps with  $\sigma(t) > 500$  m. Around 13:00 UT the positioning quality was worse than 100 m almost throughout all of Japan.

We also found latitudinal dependency of the number of positioning slips. There were practically no slips registered at the northernmost GPS receivers of the GEONET. Thus, starting from latitude 38° N there were few positioning slips. In contrast to that, the site 0080 located at 34.3° N (Fig. 13) practically did not operate from 11 to 16 UT. It is important to note that, as the station latitude increases, the  $\sigma(t)$  error generally decreases.

It was found that bubbles may propagate far on the north, although they are a typical feature of the equatorial ionosphere within  $\pm 20^\circ$  relative to the geomagnetic equator. As we showed above, due to the emergence of aspect conditions for certain navigation satellites, the positioning quality deterioration caused by the bubble is also possible at mid latitudes up to 38-39° N. The latter observation could serve as a probable explanation for the sharp worsening of positioning quality during the October 29-31, 2003 powerful geomagnetic storm at a number of GPS stations in California (30-40° N) reported by Afraimovich et al. (2009). It should be noted that the registered GPS phase losses-of-lock correspond to elevations much higher than the cut-off elevation value of  $10^\circ$ . Therefore, the registered losses-of-lock were not associated with low elevation effects.

Our results verify and supplement the results by Ma and Maruyama (2006) and Anderson and Straus (2005) and show that the aspect conditions for GPS signal propagation relative to electron density ionospheric irregularities aligned to the geomagnetic field may have a considerable effect on the performance of GPS.

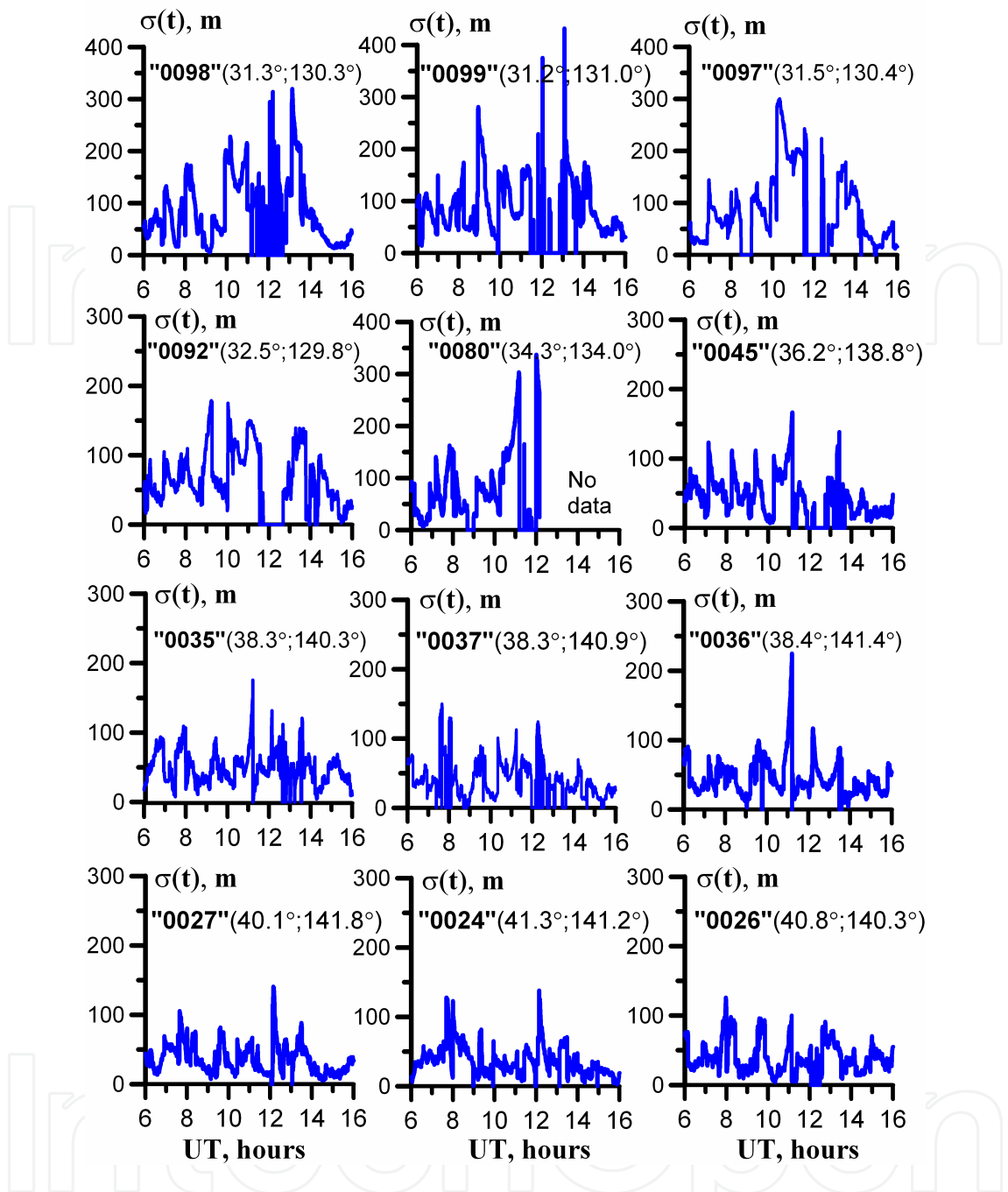


**Figure 13.** GPS positioning errors of 12 GPS GEONET stations from 6 to 16 UT on February 12, 2000. The station names and the coordinates are indicated on the panels, respectively.

#### 4. Real-time alert of sudden radio-propagation media disturbances for GNSS users

Upgrading the navigation support using global navigation satellite systems (GNSS) requires taking into account of more important effect factors, such as the large-scale disturbance of the near-Earth space environment. Influence of geomagnetic and sporadic disturbances of the

near-Earth space environment on GNSS users includes effects of regular and irregular refraction in the near-Earth space environment, interference fading (scintillation) of transionospheric signals, and dispersion distortions.

Effects of regular and irregular refraction as well as their compensation methods by the GNSS equipment algorithms were studied quite well. Application of differential modes, along with two-frequency simultaneous measurements of radio navigation parameters, allows us to compensate sufficiently their influence on operation of GNSS consumer's equipment. However, according to recent research, it has precisely irregular effects of disturbances of the near-Earth space environment that can cause deterioration in the positioning accuracy or the positioning error due either to a sharp deterioration in constellation geometry. The effect of short-term fading and dispersion distortions is equivalent to the decrease in signal-to-noise ratio in the input of phase and code tracking loops. This may result in a sharp deterioration in measurement precision of radio navigation parameters or satellite vehicle (SV) signal tracking failure (Doherty et al., 2004).

As deduced from the findings (Kintner et al., 2001), influence of multiscale ionospheric disturbances on the GNSS operation is complicated and can not be predicted. This raises the question of the near-real-time control of signal propagation medium along the line of sight of a SV in the field of view at a given time. The aim of the near-real-time control is to give immediate notice to GNSS users, allowing the GNSS consumer's equipment to be adopted for sharply changing conditions of the SV signal propagation caused by geomagnetic and sporadic disturbances of the near-Earth space environment. This can be done through the adaptation of phase and code tracking loops. Removal of SV with abnormally strong scintillations of signal parameters from the solution of navigation problem can also be done to accomplish this. In the latter case, we can consider the possibility of giving notice of the propagation medium state as part of Receiver Autonomous Integrity Monitoring (RAIM) algorithms.

The aim of Section 4 is to analyze the possibility using the index of ionospheric scintillations of transionospheric signal power ( $S_4$ ) for online control of the integrity of measurements of radio navigation parameters with the use of signals from some SV under disturbed geomagnetic conditions of propagation medium of GNSS signals.

#### **4.1. Connection between the scintillation index and TEC variations during multiscale ionospheric disturbances**

According to modern opinion, electron density (ED) disturbances in the ionosphere are the superposition of compression - rarefaction waves with periods from tenths of minutes to 1-2 hours. Fig. 14 presents typical logarithmic power spectra of travelling ionospheric disturbances (TIDs)  $\lg S^2$  obtained from GPS observations on July 29, 1999 (313 LOS) under quiet geomagnetic conditions and during the strong magnetic storm of July 15, 2000 (197 LOS) (Afraimovich and Perevalova, 2006).  $k$  is the spectrum slope,  $F$  is the TEC variation frequency,  $T$  is the period of variation and  $\Lambda$  is the wavelength (mean chosen velocity was 100 m/s).

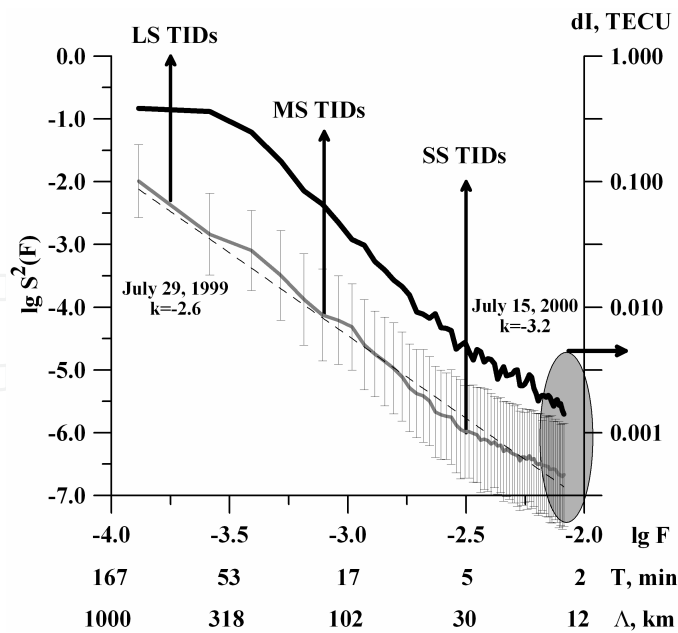


**Figure 14.** Characteristic spectrum of ionospheric disturbances under quiet and disturbed geomagnetic conditions (Afraimovich and Perevalova, 2006). The thick gray curve stands for quiet conditions, the black curve denotes disturbed conditions, and the dashed line is approximation of gray curve. Root-mean-square deviations are represented as grey segments.

According to Figure 14, intensity of ED irregularities of all spatial-temporal scales increases under disturbed geomagnetic conditions. In this case, spectral slope varies insignificantly, which suggests a proportional energy redistribution of geomagnetic disturbance under the ionospheric disturbances at all scales. The major portion of disturbance energy corresponds to large-scale and medium-scale TIDs (LS TIDs and MS TIDs, respectively). Such disturbances introduce smooth refraction errors of ranging to the GNSS equipment.

Small-scale TIDs (SS TIDs) may cause fast fluctuations of the refraction ionospheric ranging error. However, the main contribution to degradation of SV signals is made by scintillations of the radio signal received on earth due to diffraction on small-scale ED irregularities with a size of about one radius of the first Fresnel zone. The oval and horizontal arrows in Fig. 14 depict the region of these small-scale ionospheric inhomogeneities. According to recent research, such inhomogeneities accompanying magnetic storms are generated not only in low and high but also in middle latitudes (Demyanov et al., 2012; Afraimovich et. al., 2009b).

Smooth refraction effects caused by LS and MS TIDs can be effectively removed by two-frequency measurements of radio navigation parameters or by using differential GNSS mode. As for fast refraction variations and especially ionospheric scintillations, ranging errors or signal tracking failures caused by these events can not be corrected effectively due to the two-frequency measurements or the differential mode.

The most effective way out is to develop methods and algorithms for online detection of these events and giving immediate notice to GNSS users. This requires a universal index that could

relate to the quality of radio navigation measurements to the current conditions of radio wave propagation in the Earth's ionosphere, given small-scale ED irregularities.

According to the results by Bhattacharyya et al. (2000), it is possible to use the scintillation index S4 for this purpose. Bhattacharyya et al. (2000) have established functional relationship between variations in integral parameter of the propagation medium - the total electron content along the line of sight of a satellite - and corresponding variations in the scintillation index at the receiving point. Such approach to determining ionospheric scintillations of SV signal parameters is based on the phase screen method. According to this method, variations in the carrier phase are related to TEC variations along the signal propagation trajectory ( $x$ ) through a thin layer, containing ED irregularities, in the following way:

$$\Delta\phi(x) = -\lambda \cdot r_e \cdot \Delta I(x) \quad (19)$$

where  $\lambda$  is the wavelength,  $r_e$  is the classical electron radius. The complex amplitude of SV signals at the receiving point ( $x, z$ ) results from the addition of partial waves to phases  $\Delta\phi_i(x)$ :

$$u(x, z) = \sqrt{\frac{j}{\lambda \cdot z}} \cdot \int_{-\infty}^{\infty} u_i(x', 0) \cdot \exp\left[\frac{-j\pi(x-x')^2}{\lambda \cdot z}\right] dx' \quad (20)$$

$$u_i(x, 0) = U_{0,i} \cdot \exp(-j\Delta\phi_i(x))$$

where  $u_i(x, 0)$  is the amplitude of partial wave immediately after it emerges from the ionospheric irregularity layer,  $z$  is the distance from the scattering irregularity layer to the receiving point,  $x'$  is the current point coordinate along the irregularity layer.

Using the above-mentioned conception of the multiscale structure of ionospheric disturbances, we can easily determine contribution of the SV signal diffraction on ED irregularities to ionospheric scintillations and fast refraction fluctuations of SV signal parameters. For this purpose we can apply the Fourier transform to the complex amplitude (4.2), and the complex amplitude of the SV signal at the receiving point will be as follows:

$$u_F(q, z) = U_F(q, 0) \cdot \exp(-j \cdot \pi \cdot \lambda \cdot z \cdot q^2), \quad (21)$$

where  $1/q$  is the spatial scale of ED irregularities in the layer. Given only large-scale disturbances whose sizes are much more than the first Fresnel zone  $1/q \gg d_F = \sqrt{2\lambda \cdot z}$ , there will be only slow refraction phase variations (caused by the drift of the large-scale ED inhomogeneity relative to the wave propagation trajectory) in the complex amplitude, at the receiving point  $u_F(q, z)$ . That is why  $u_F(q, z) \approx U_F(q, 0)$ .

If, along with large-scale inhomogeneities, there are smaller-scale inhomogeneities, the complex amplitude at the receiving point  $u_r(q,z)$  depends on exponential factor being a part of expression (20). According to (19-21), variations in the SV signal amplitude at the receiving point can be expressed through TEC variations. Contribution of ED irregularities having different scales is integrated along the line of sight.

Besides, it must be borne in mind that the propagation trajectories of the SV signal and ED irregularities move with respect to each other. To take this into account, TEC spatial variations along the 'receiver-satellite' line-of-sight should be transformed into temporal ones.

In the phase-screen approximation, variations in the signal phase and amplitude at the receiving point are interconnected (Bhattacharyya, 1999):

$$\frac{d^2}{dx^2}\phi(x,z) = \frac{2\pi}{\lambda \cdot z} \left[ 1 - \frac{\varepsilon(x,z)}{\varepsilon_0} \right]. \quad (22)$$

where  $\varepsilon = u(x,z)^*$  and  $\varepsilon_0$  are wave intensities before (i.e. undisturbed intensity) and after propagation through the irregularity layer. According to (19), phase variations can be directly related to TEC variations. At the receiving point, variations of the wave phase are caused by relative motion of ED irregularities at a velocity  $v$ . Spatial variations can be thus expressed through temporal ones. With this end in view change in space coordinate  $x$  should be expressed through velocity  $v$  (Bhattacharyya, 1999)

$$\frac{d^2}{dt^2}\Delta I(t) = -\frac{2\pi}{\lambda \cdot r_e} \frac{v^2}{\lambda \cdot z} \left[ 1 - \frac{\varepsilon(t,z)}{\varepsilon_0} \right], \quad (23)$$

where  $v$  is the relative velocity of motion of ED irregularities and wave propagation trajectories.

The scintillation index S4 is the root-mean-square deviations of variations in normalized series  $\frac{\varepsilon(t,z)}{\varepsilon_0}$ . Consequently, the equation (23) determines ionospheric scintillations of the SV signal amplitude, caused by TEC variations along the line-of-sight. The scintillation index S4 can be thus considered as a valid index of current conditions of the SV signal propagation through medium, given disturbances of different scales.

#### 4.2. Analysis of the S4 index, TEC variations and positioning quality during a magnetic storm

In this section, we analyze applicability of the S4 index to immediate estimation of navigation measurement quality under disturbed geomagnetic conditions. We used experimental measurements of coordinates of the ISTP stationary station (Institute of Solar-Terrestrial Physics, Irkutsk, 52.2° N, 104.4° E, magnetic latitude is 41°) for analysis. Measurements were made with the GPS/GLONASS single-frequency navigation receiver MRK-19L. The equipment

was installed at ISTP under stationary laboratory conditions. Geodetic survey of external antenna of MRK-19L was made with ASHTECH Z-XII3T, a dual-frequency GPS receiver. To measure TEC along the 'receiver - GPS satellite' line-of-sight we used data at the IRKT station of IGS network (<http://garner.ucsd.edu/>). The distance between ISTP and IRKT is 5 km so the ionosphere can't be changed significantly. Therefore we assumed that LOS was practically the same.

The experimental bench consists of:

- single-frequency receiver MRK-19L,
- computer controlling the operation mode of MRK-19L (control computer),
- computer registering measurement data (registration computer - R-comp).

Special software designed for MRK-19L was installed on the control computer. The software chose an operation mode of MRK-19L. Besides, the special software was responsible for communications protocol and mode between MRK-19L and R-comp. From the receiver, measurement data came to R-Comp in binary format. We have developed software to record data and installed it on R-Comp. The registration software includes a block of primary data logging and a block of reprocessing and analysis.

The programme of primary data logging performs data conversion. These data come to COM port of the R-Comp in a standard, unified data interchange format NMEA-0183. The period of data record in the primary file is 4 s. Then counts of the time of registration and of the receiver's current geodetic coordinates are extracted from the primary data file with the use of the block of reprocessing and analysis. Afterwards these coordinates are converted to rectangular geocentric coordinates.

We chose November 9, 2004 for analysis. On this day, we observed a complicated geomagnetic disturbance of the ionosphere caused by the solar flares of November 3 (01.24-01.44 UT) and November 5 (11.26-11.41 UT). On November 7, 2004, an abrupt drop in dynamics of the horizontal component H of the geomagnetic field was recorded at 22.00-24.00 UT. On November 9, 2004, moderate disturbances of the geomagnetic field were observed. In the time interval 20.00- 21.00 UT, there was a strong disturbance of the geomagnetic field once again; it was caused by the solar flare of November 5, 2004. Consequently, the day we analysed is characterised by a whole gamut of perturbing factors which affected near-Earth space and positioning accuracy.

There was increase in ED in the F layer from 14.00 to 20.00 UT on November 9, 2004. On the next day, however, such ED disturbances were not observed. The main contribution to ionospheric scintillations is made by disturbances in the F region. Consequently, we may assume that there were favourable conditions for formation of such scintillations on November 9.

The decrease in the average (of all satellites under observation) signal level at the receiving point can serve as a manifestation of intense ionospheric scintillations. To prove this, we analysed series of measurements of the SV signal-to-noise for each hour of observation. In

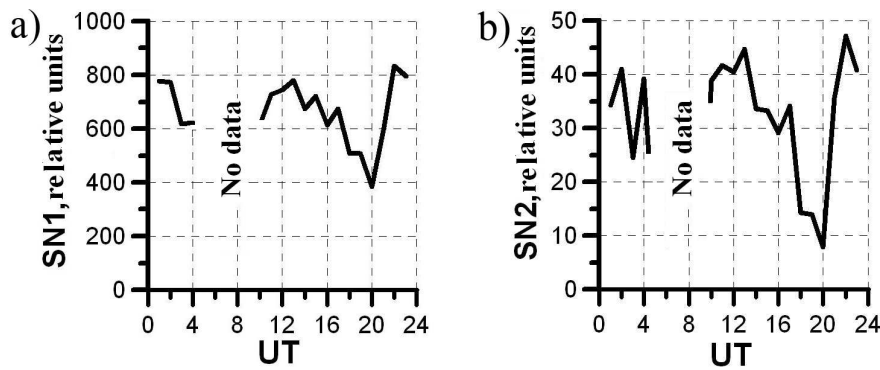


**Figure 15.** Averaged values of the SV signal level with elevation angles  $\theta$  of more than  $60^\circ$  on November 9, 2004.

order to provide reliable detection of the effect, we considered measurements for which elevation angle  $\theta$  was more than  $60^\circ$ . Because of this, the strength of effects at low elevation angles (whereat the signal attenuation can be related not only to ionospheric disturbances) decreases.

Results are presented in Fig. 15. SN1 (a) is signal-to-noise at L1 and SN2 (b) is the same at L2. From 4.30 to 9.50 UT, there were no SV with elevation angles  $\theta$  of more than  $60^\circ$  over the observation site. A steady decrease in the signal level of both operating frequencies of SV is observed at the observation site from 17.00 to 21.00 UT. It coincides in time with occurrence of intense ionospheric disturbances caused by the magnetic storm.

The decrease in signal-to-noise ratio at the receiving point due to ionospheric scintillations may lead to deterioration in positioning quality. Fig. 16a presents series of errors in the positioning of ISTP -  $\Delta S = \sqrt{\Delta X^2 + \Delta Y^2 + \Delta Z^2}$ . Measurements were made with MRK-19L, on the basis of GPS data only. The time step was 4 s. A sharp increase in positioning errors was observed from 15.00 to 20.30 UT. This period corresponds to the local night (23.00-04.30 LT) and is marked by rectangle in Fig. 16a.

Notice that the said deterioration in the positioning precision correlates well (according to the occurrence time) with appearance of regions with increased ED. Besides, the period of increase in positioning errors coincides with the period of decrease in the SV signal level at both GPS frequencies (Fig. 15).

To extract effects caused by deterioration in geometry of constellation of satellites, we calculated Position Dilution of Precision (PDOP). Fig. 16b presents PDOP values for ISTP. The time step was 4 s. The maximum PDOP values were observed at 01.10 and 02.20 UT. This was due to the local peculiarity of the observation site. Note that the increase in positioning errors did not coincide with the maximum PDOP values. From 15.00 to 20.30 UT, we observed only short-term increases ( $> 3.5$ ) in PDOP values. Thus, ionospheric scintillations of the SV signal amplitude were most likely to make the most substantial contribution to the increase in positioning errors during the period under consideration.

Fig. 17 exemplifies TEC observations made by GPS satellites PRN 06 and PRN 20 on November 9, 2004 at 00.00-03.00 UT. The figures also present the S4 index dynamics (see Fig. 17c,f). Time

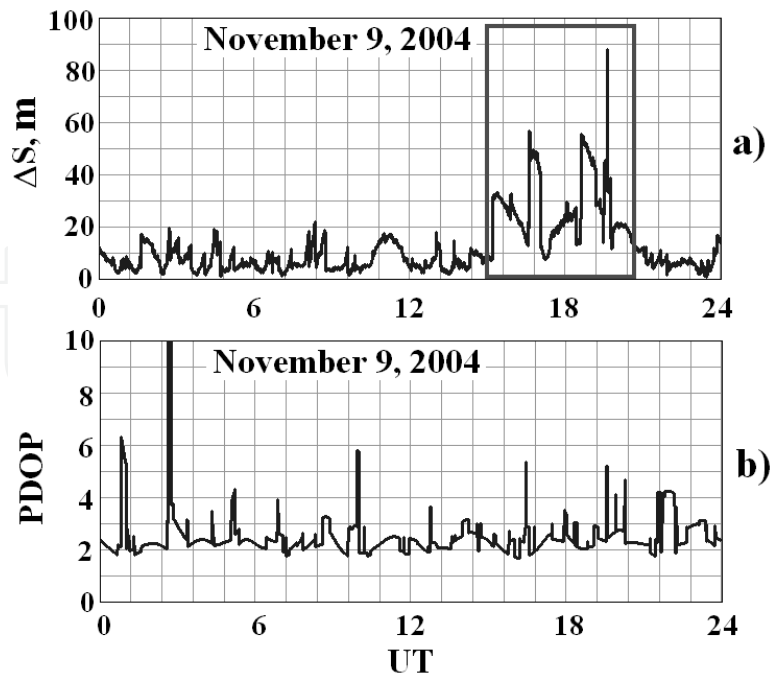


**Figure 16.** Positioning errors (a) and Position Dilution of Precision (b) during the magnetic storm on November 9, 2004. Data from MRK-19L were used for positioning.

series of TEC variations with eliminated trend are given in Fig. 17a,d. The method to eliminate the trend is described in (Afraimovich and Perevalova, 2006). We calculated TEC values with the use of two-frequency phase measurements. The values were measured with ASHTECH Z-XII3T (IRKT). The time step was 30 s. Fig. 17b,e illustrate series of the time derivative of TEC. The scintillation index was calculated using MRK-19L measurements of signal-to-noise ratio at the GPS L1 frequency.

$$S4^2 = \frac{\langle P^2 \rangle - \langle P \rangle^2}{\langle P \rangle^2}, \quad (24)$$

where  $P$  is the current value of signal-to-noise ratio measured in relative units and the time step is 4 s. When calculating the scintillation index, averaging of measurements of signal  $P$  amplitude was made in the time interval of 28 s in order to coordinate TEC measurements and estimate  $S4$  values in time.

According to Fig. 17a-c, short-period TEC disturbances corresponding to small-scale ED irregularities are quite insignificant in this case. Smooth TEC variations are more significant. This is also the case for small values of the  $S4$  index ( $S4 \leq 0.1$ ).

Fig. 17d-f presents data from GPS PRN 06. As can be seen, fast TEC variations caused by small-scale ED irregularities are dominant. Consequently, high values of the  $S4$  index ( $\geq 0.8$ ) are observed (Fig. 17 f). We can draw a conclusion that, in the conditions under consideration, the  $S4$  index reflects disturbances of propagation medium of SV signals quite reliably. The analysis

substantiates the validity of using the S4 index under disturbed geomagnetic conditions. In this case, we observed superposition of effects of several geomagnetic disturbances of radio wave propagation medium. Thus, the S4 index can be applied to making online control of the quality of measurements of radio navigation parameters during magnetic storms.

There are, however, a number of restrictions that have not been taken into consideration. These restrictions should be considered individually. Noteworthy is the fact that velocity  $v$  and integration time of the right-hand and left-hand sides of equation (23) are undetermined parameters. These parameters may reliably reflect the current conditions of radio wave propagation.

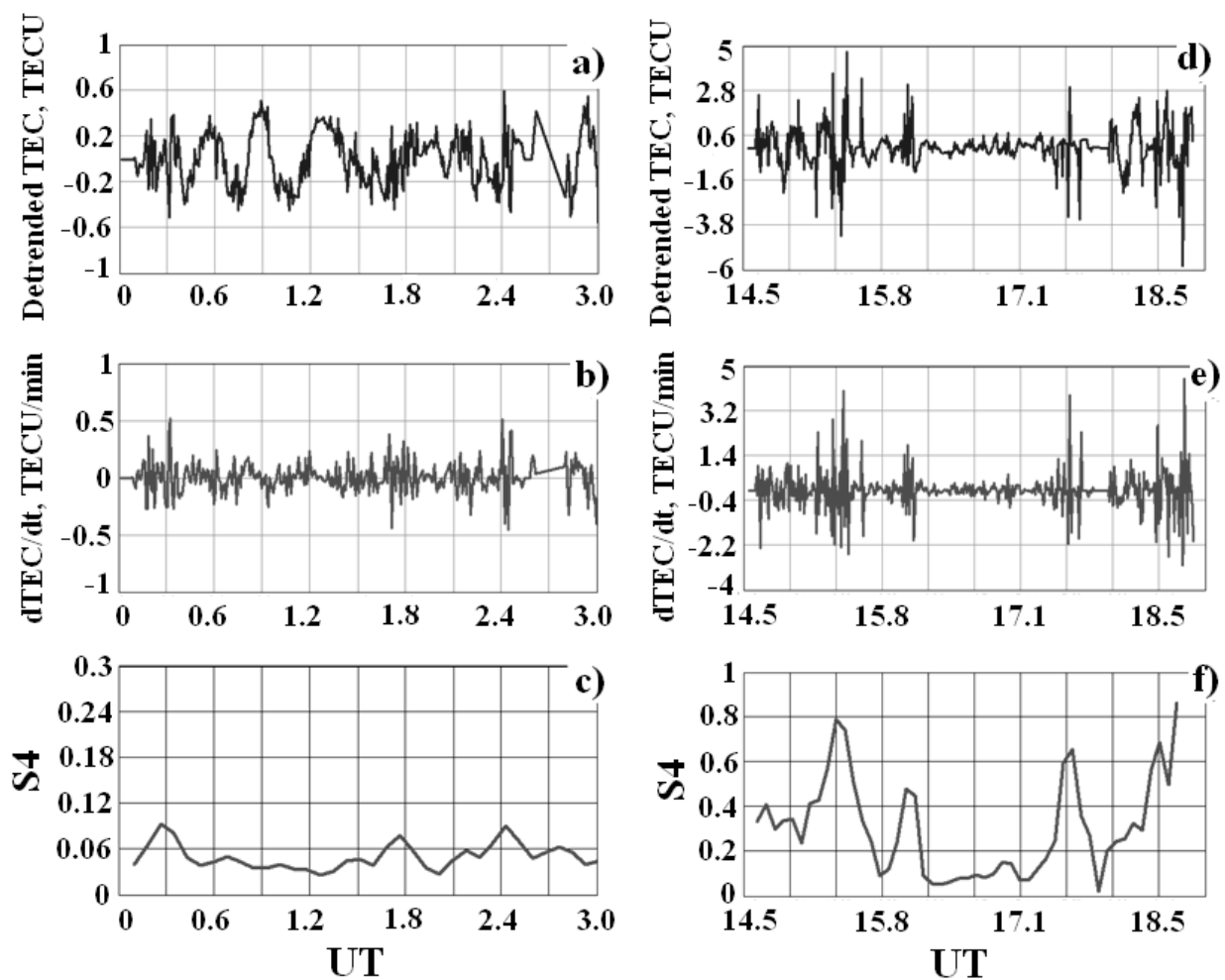


**Figure 17.** TEC variations (a, d), TEC derivative (b, e), and the S4 index (c, f). Data from the GPS satellite PRN 20 (a-c) and PRN 06 (d-e) were used.

The article deals mainly with ionospheric scintillations caused by the SV signal diffraction. The main contribution is made by ED irregularities with the scale of about the first Fresnel zone  $d_F \approx \sqrt{2\lambda \cdot z}$ . In this case, the integration time can be determined from relative velocity  $v$ . The

Fresnel frequency  $v_F$  (related to velocity  $v$ ) corresponds to the magnitude inversely proportional to the characteristic scintillation period.

$$v_F = \frac{v}{\sqrt{2\lambda \cdot z}} \quad (25)$$

However, it is a common knowledge that the Fresnel frequency can vary over a wide range. For operating GPS frequencies, typical sizes of inhomogeneities located at 110-400 km that make the main contribution to amplitude scintillations are in the range 145 to 310 m. The GPS satellite moves in a circular orbit at 20200 km. The revolution period is 12 hours. If the line of sight is zenith-directed, the horizontal component of the rate of motion of the SV signal trajectory is 21 m/s for the E region and 77 m/s for the F region. The horizontal drift velocity of small-scale ED irregularities in middle latitudes is usually more than 150 m/s (Afraimovich et al., 2004). Consequently, the Fresnel frequency value can vary from 0.08 to 0.36 Hz. In high latitudes, the drift velocity can be up to 1 km/s. In this case, the Fresnel frequency can be significantly higher (Bhattacharyya et al., 2000; Afraimovich et al., 2004). Consequently, we should also analyse time of averaging of observational data that enter into the left-hand and right-hand sides of equation (23) to estimate adequately the current conditions of scintillation formation.

The restriction can be insignificant, if the phase-screen approximation is adequate. According to (Bhattacharyya et al., 2000), equation (23) can be replaced by the following empirical expressions:

$$DROTI = \alpha \cdot v_F \cdot S4$$

$$DROTI = \sqrt{\left\langle \left( \frac{d^2}{dt^2} \Delta I(t) \right)^2 \right\rangle - \left\langle \frac{d^2}{dt^2} \Delta I(t) \right\rangle^2}, \quad (26)$$

where  $\alpha$  is the empirical parameter chosen for current observational conditions. In (Bhattacharyya et al., 2000, Bhattacharyya, 1999), it was found that  $\alpha = 1.6 \cdot 10^3 - 8.5 \cdot 10^3$ .

The phase screen approximation is not applicable when waves pass through the layer of inhomogeneities having high intensity and thickness. This is the case for the low-latitude and equatorial ionosphere. In the case under consideration, we have observed saturation of amplitude scintillations. If the irregular layer is thick, amplitude fluctuations are developed inside of it. As a result, the wave becomes subject to both phase and amplitude disturbances in the ionospheric layer output (Yeh and Liu, 1982). The well-known observational results show that amplitude scintillations were usually registered in such cases. Scintillations of the phase, angle of arrival and polarisation of received radio emission were observed much less often (Gunze, 1982). In this case, the S4 index determined only intensity of amplitude scintillations. These data are not enough to give immediate notice to GNSS consumers of a sharp

deterioration in conditions of radio wave propagation. There are known cases of tracking loss of SV signals due to abrupt changes in the carrier phase. Noteworthy is the fact that variations in the signal amplitude are relatively low (Afraimovich et al., 2009b).

Additional research is needed to find new indices of signal propagation medium under different conditions. These indices should reflect variations in other parameters of the SV signal. The analysis should include influence of fluctuations of different radio-signal parameters on stability of system operation.

## Acknowledgements

The authors are grateful a lot to Prof. E.L. Afraimovich, who will never see this text, sad to say. These results couldn't be obtained without him. Authors express profound gratitude to Prof. G. Y. Smolkov for his support and interest in this investigation. We are thankful to N.S. Gavriluk, A.B. Ishin, Prof. M.V. Tinin for their assistance in the preparing some parts. We are obliged to Dr. V. V. Grechnev for his help in using the 1 GHz and 2 GHz data of the Nobeyama Radio Polarimeters and colleagues from the Nobeyama Radio Observatory for solar radio emission data on December 13, 2006, as well as the International GNSS service and Geographical Survey Institute of Japan for RINEX data. The study was partially supported by RFBR (under grant No. 12-05-33032 a), by the Ministry of Education and Science of the Russian Federation (under agreement Nos. 8699, 8388, and 14.518.11.7065) and the Russian Federation President Grant MK-2194.2011.5.

## Author details

Vladislav V. Demyanov<sup>1\*</sup>, Yury V. Yasyukevich<sup>2</sup> and Shuanggen Jin<sup>3</sup>

\*Address all correspondence to: sword1971@yandex.ru

1 Irkutsk State Railway University, Russia

2 Institute of Solar-Terrestrial Physics, the Russian Academy of Sciences, the Siberian Branch, Irkutsk, Russia

3 Shanghai Astronomical Observatory, Chinese Academy of Sciences, Shanghai, China

## References

- [1] Afraimovich, E. L. (2000). GPS global detection of the ionospheric response to solar flares // *Radio Sci.*, N 6, , 35, 1417-1424.

- [2] Afraimovich, E. L, & Perevalova, N. P. (2006). GPS monitoring of the Earth's upper atmosphere. Irkutsk. in Russian)., 480.
- [3] Afraimovich, E. L, Lesyuta, O. S, Ushakov, I. I, & Voeykov, S. V. (2002). Geomagnetic storms and the occurrence of phase slips in the reception of GPS signals // *Ann Geophys*, N 1, , 45, 55-71.
- [4] Afraimovich, E. L, Astafieva, E. I, Bergardt, O. I, Lesyuta, O. S, Demyanov, V. V, Kondakova, T. N, & Shpynev, B. G. (2004). Mid-latitude amplitude scintillation of GPS signals and GPS performance slips at the auroral oval boundary // *Radiophysics and Quantum Electronics*, N 7, , 47, 453-468.
- [5] Afraimovich, E. L, Demyanov, V. V, Ishin, A. B, & Smolkov, G. Y. (2008). Powerful solar radio bursts as a global and free tool for testing satellite broadband radio systems, including GPS-GLONASS-GALILEO // *J Atmospheric and Solar-Terrestrial Phys*, , 70, 1985-1994.
- [6] Afraimovich, E. L, Demyanov, V. V, & Kondakova, T. N. (2003). Degradation of performance of the navigation GPS system in geomagnetically disturbed conditions // *GPS Solut.*, N 2, , 7, 109-119.
- [7] Afraimovich, E. L, Demyanov, V. V, & Smolkov, G. Ya. ((2009a). The total failures of GPS functioning caused by the powerful solar radio burst on December 13, 2006 // *Earth, Planets and Space*, , 61, 637-641.
- [8] Afraimovich, E. L, Astafieva, E. I, Demyanov, V. V, & Gamayunov, I. F. Amplitude Scintillation of GPS Signals and GPS Performance Slips // *Adv. Space Res.* , 43, 964-972.
- [9] Anderson, P. C, & Straus, P. R. (2005). Magnetic field orientation control of GPS occultation observations of equatorial scintillation // *Geophys. Res. Lett.*, doi: 10.1029/2005GL023781., 32, L21107.
- [10] Astafyeva, E. I, Afraimovich, E. L, & Voeykov, S. V. (2008). Generation of secondary waves due to intensive large-scale AGW traveling // *Adv. Space Res.*, , 41, 1459-1462.
- [11] Bhattacharyya, A, Beach, T. L, Basu, S, & Kintner, P. M. (2000). Nighttime Equatorial Ionosphere: GPS Scintillations and Differential Carrier Phase Fluctuations // *Radio Sci.*, , 35, 209-224.
- [12] Bhattacharyya, A. (1999). Deterministic retrieval of ionospheric phase screen from amplitude scintillations // *Radio Sci.*, , 34, 229-240.
- [13] Burke, W. J, Donatelli, D. E, Sagalyn, R, & Kelley, M. (1979). Low density regions observed at high altitudes and their connection with equatorial spread F // *Planet. Space Sci.*, , 27, 593-601.

- [14] Carrano, C. S, Groves, K. M, & Bridgwood, C. T. (2007). Effects of the December 2006 Solar Radio Bursts on the GPS Receivers of the AFRL-SCINDA Network // In: Doherty PH (ed) Proc International Beacon Satellite Symp, June , 11-15.
- [15] Cerruti, A. P, Kintner, P. M, Gary, D. E, Lanzerotti, L. J, De Paula, E. R, & Vo, H. B. (2006). Observed Solar Radio Burst Effects on GPS/WAAS Carrier-to-Noise Ration. // Space Weather, doi:10.1029/2006SW000254., 4, S10006.
- [16] Chen, Z, Gao, Y, & Liu, Z. (2005). Evaluation of solar radio bursts' effect on GPS receiver signal tracking within International GPS Service network // Radio Sci, doi: 10.1029/2004RS003066., 40, RS3012.
- [17] Conker, R. S, Arini, M. B, Hegarty, J, & Hsiao, T. (2003). Modeling the effects of ionospheric scintillation on GPS/satellite-based augmentation system availability // Radio Sci., N 1, P. P. 1001, doi:10.1029/2000RS002604., 38
- [18] ICD-GLONASS ((2002). Global navigation satellite system-GLONASSInterface Control Document (in Russian). [http://www.glonassgsm.ru/upl\\_instructions/ICD-2002r.pdf](http://www.glonassgsm.ru/upl_instructions/ICD-2002r.pdf)
- [19] Demyanov, V. V. Yasyukevich Yu.V., Ishin A.B., Astafyeva E.I.. ((2012). Effects of ionosphere super-bubble on the GPS positioning performance depending on the orientation relative to geomagnetic field // GPS solutions, N 2, DOI:s10291-011-0217-9., 16, 181-189.
- [20] Doherty, P, Coster, A. J. A, & Murtagh, W. (2004). Space Weather Effects of October-November 2003 // GPS Solutions, , 8, 267-271.
- [21] Gurtner, W, & Estey, L. (2009). RINEX: The Receiver Independent Exchange Format. Version 3.01. June 2009. Available from <<http://igsceb.jpl.nasa.gov/igsceb/data/format/rinex301.pdf>>.
- [22] Gunze, E, & Zhaohang, L. (1982). The Ionospheric radiowave scintillations // TIHER, N.4, , 70, 5-45.
- [23] Icd-gps, c. (1993). Interface Control Document. <http://www.navcen.uscg.gov/pubs/gps/icd200/ICD200Cw1234.pdf>
- [24] Hewish, A, & Symons, M. D. (1969). Radio investigations of the solar plasma // Planet. Space Science, N 3, , 17, 313-320.
- [25] Huang, C, Foster, S, & Sahai, J. C. Y. ((2007). Significant depletions of the ionospheric plasma density at middle latitudes: A possible signature of equatorial spread F bubbles near the plasmopause // J. Geophys. Res., , 112, A05315.
- [26] Jin, S. G, Luo, O, & Park, P. (2008). GPS observations of the ionospheric F2-layer behavior during the 20th November 2003 geomagnetic storm over South Korea // J. Geod., N 12, doi:s00190-008-0217-x., 82, 883-892.

- [27] Kaplan, E. D. ed) ((1996). Understanding GPS: Principles and applications. Artech House, 556 p.
- [28] Kelley, M. C, Makela, J. J, Paxton, L. J, Kamalabadi, F, Comberiate, J. M, & Kil, H. (2003). The first coordinated ground- and space-based optical observations of equatorial plasma bubbles // *Geophys. Res. Lett.*, N 14, doi:10.1029/2003GL017301., 30, 1766-1769.
- [29] Kintner, P. M, & Ledvina, B. M. (2005). The ionosphere, radio navigation, and global navigation satellite systems // *Adv. Space Res.*, N 5, , 35, 788-811.
- [30] Kintner, P. M, Kil, H, & De Paula, E. (2001). Fading Time Scales Associated with GPS Signals and Potential Consequences // *Radio Science*, N 4, , 36, 731-743.
- [31] Kintner, P. M, Ledvina, B. M, De Paula, E. R, & Kantor, I. J. (2004). Size, shape, orientation, speed, and duration of GPS equatorial anomaly scintillations // *Radio Sci.*, doi: 10.1029/2003RS002878., 39, RS2012.
- [32] Kintner, P. M, Humphreys, T, & Hinks, J. (2009). GNSS and ionospheric scintillation. How to Survive the Next Solar Maximum // *Inside GNSS*, N 4, , 4, 22-31.
- [33] Klobuchar, J. A, Kunches, J. M, & Van Dierendonck, A. J. (1999). Eye on the ionosphere: Potential solar radio burst effects on GPS signal to noise // *GPS Solut.*, N 2, , 3, 69-71.
- [34] Ledvina, B. M, & Makela, J. J. (2005). First observations of SBAS/ WAAS scintillations: Using collocated scintillation measurements and all-sky images to study equatorial plasma bubbles // *Geophys. Res. Lett.*, doi:10.1029/2004GL021954., 32, L14101.
- [35] Ledvina, B. M, Makela, J. J, & Kintner, P. M. (2002). First observations of intense GPS L1 amplitude scintillations at midlatitude // *Geophys. Res. Lett.*, N 14, DOI:GL014770., 29
- [36] Ledvina, B. M, Kintner, P. M, & Makela, J. J. (2004). Temporal properties of intense GPS L1 amplitude scintillations at midlatitudes // *Radio Sci.*, doi: 10.1029/2002RS002832., 39, RS1S18.
- [37] Ma, G, & Maruyama, T. (2006). A super bubble detected by dense GPS network at east Asian longitudes // *Geophys. Res. Lett.*, DOI:GL027512., 33, L21103.
- [38] Manchester, R. N, & Taylor, J. H. (1977). Pulsars. Freeman, San Francisco, 176 pp.
- [39] Maurits, S. A, Gherm, V. E, Zernov, N. N, & Strangeways, H. J. (2008). Modeling of scintillation effects on high-latitude transionospheric paths using ionospheric model (UAF EPPIM) for background electron density specifications // *Radio Sci.*, DOI: 10.1029/2006RS003539., 43, RS4001.
- [40] McClure, J. P, Hanson, W. B, & Hoffman, J. H. (1977). Plasma bubbles and irregularities in the equatorial ionosphere // *J. Geophys. Res.*, , 82, 2650-2656.

- [41] Meggs, R. W, Cathryn, N. M, & Smith, A. M. (2006). An investigation into the relationship between ionospheric scintillation and loss of lock in GNSS receivers // Proceedings of the Meeting RTO-MP-IST-056 Characterising the Ionospere. Paper 5. Alaska, Fairbanks, US, June , 12-16.
- [42] Obara TOya H. ((1994). EXOS-B (Jikiken) observations of the field aligned plasma density depletion at high altitude region // in Low-Latitude Ionospheric Physics CO-SPAR Colloquia Sen, 7, edited by F.-S. Kuo, Elsevier, New York, 1994, 275 pp.
- [43] Pätzold, M, Neubauer, F. M, & Bird, M. K. (1995). Radio occultation studies with Solar Corona Sounders // Space Science Reviews, , 77-80.
- [44] Perov, A. I, & Kharisov, V. N. (2005). GLONASS: Principles of Construction and Functioning. Radiotekhnika, Moscow, 720 pp. (in Russian).
- [45] Skone, S. H. (2001). The impact of magnetic storms on GPS receiver performance // Geodesy, N 9-10, doi:10.1007/S001900100198,, 75, 457-468.
- [46] Skone, S, & De Jong, M. (2001). Limitations in GPS receiver tracking performance under ionospheric scintillation // Physics and Chemistry of the Earth. Part A, N 6-8, , 26, 613-621.
- [47] Tereshchenko, E. D, Milichenko, A. N, Frolov, V. L, & Yurik, R. Yu. ((2008). An observation of the magnetic zenith effect by using GPS/GLONASS satellites signals // Radiophysics and Quantum Electronics, N 11, , 51, 842-846.
- [48] Tsui, J. B. (2005). Fundamentals of global positioning system receivers: a software approach.- 2nd ed. 0-47170-647-7G109.5.T85 2005.
- [49] Wernik, A. W, Liu, C. H, Franke, S. J, & Gola, M. (1990). High-latitude irregularity spectra deduced from scintillation measurements // Radio Sci., N 5, , 25, 883-895.
- [50] Woodman, R. F. LaHoz C. ((1976). Radar observations of F region irregularities // J. Geophys. Res., , 81, 5447-5466.
- [51] Yeh, K. C, & Liu, C. H. (1982). Radio wave scintillations in the ionosphere // Proc. IEEE, N 4, , 70, 24-64.
- [52] Zhuk, N. (1980). Scintillation studies of cosmic source angular structure (Review) // Radiophysics and Quantum Electronics, N 8, , 23, 597-615.